Universidade de Aveiro Departamento de Engenharia Cerâmica e do Vidro
2011

Swagata Dutta

Influência da alteração da trajectória de deformação no comportamento mecânico do Mg

Influence of the strain path change on the mechanical behavior of Mg

Universidade de Aveiro Departamento de Engenharia Cerâmica e do Vidro
2011

Swagata Dutta

Influência da alteração da trajectória de deformação no comportamento mecânico do Mg

Influence of the strain path change on the mechanical behavior of Mg

Dissertação apresentada à Universidade de Aveiro para cumprimento dos requisitos necessários à obtenção do grau de Mestre em Ciência dos Materiais, realizada sob a orientação científica do Doutor Joaquim Manuel Vieira Professor Catedrático do Departamento de Engenharia Cerâmica e do Vidro da Universidade de Aveiro e do Doutor Augusto Luís Barros Lopes, Professor Auxiliar do Departamento de Engenharia Cerâmica e do Vidro da Universidade de Aveiro.

Dissertation presented to University of Aveiro for the requirement of partial fulfillment of the Masters of Science degree in materials science under supervision of Doctor. Joaquim Manuel Vieira, Full Professor in the Department of Ceramic and Glass Engineering of the University of Aveiro and Doctor. Augusto Luís Barros Lopes, Auxiliary Professor in the Department of Ceramic and Glass Engineering of the University of Aveiro.

o júri

Presidente	Prof. Dr. Maria Margarida Tavares Lopes de Almeida, Professora Auxiliar da Universidade de Aveiro
Arguente	Prof. Dr. Manuel Fernado Gonçalves Vieira, Professor Associado da Faculdade de Engenharia da Universidade do Porto
Orientador	Prof. Dr. Joaquim Manuel Vieira, Professor Catedrático da Universidade de Aveiro
Co-orientador	Prof. Dr. Augusto Luís Barros Lopes, Professor Auxiliar da Universidade de Aveiro

acknowlegments

I am very thankful to my supervisor Prof. Dr. Joaquim Manuel Vieira and co-supervisor Prof. Dr. Augusto Luis Barros Lopes for their guidance and support from the initial to the final stage which enabled me to develop an understanding of the subject and writing the thesis.

I would like to extend my gratitude to Prof. Dr.-Ing. Joachim Albrecht for his time in co-supervising my work and his guidance under Erasmus Mundus in Materials Science program.

I am also very grateful to Prof. Drª Gabriela Tamara Vincze for her assistance during all mechanical experiments and useful advice and helpful suggestions in processing the obtained mechanical results.

The free access to granted by Prof. Dr. Abel Dias dos Santos to the Instron 4208 Universal testing machine of INEGI, University of Oporto, is grateful acknowledged

I would like to thank the EMMS consortium for the unforgettable program and the European Commission for the scholarship.

I would like to thank to acknowledge of RNME – Pole University of Aveiro (FCT Project RED/1509/RME/2005) for instrument use, scientific and technical assistance.

palavras-chave

Liga de magnésio AZ31, anisotropia plástica, microestrutura de deslocações, textura cristalográfica, modelo visco-plástico auto-consistente.

resumo

Neste trabalho foi investigado o efeito da alteração da trajectória de deformação no comportamento mecânico da liga de magnésio AZ31 através de ensaios sequenciais de tracção uniaxial realizados à temperatura ambiente.

A pré-deformação foi realizada na direcção de laminagem inicial da chapa (RD) até um valor de deformação plástica igual a 0,07. Das amostras pré-deformadas, foram cortados provetes a 0º, 15º, 30º, 45º, 60º, 75º e 90º de RD que foram submetidos a recarga em tracção uniaxial.

A influência da microestrutura de deslocações e da textura cristalográfica desenvolvidas durante a deformação plástica no comportamento do material durante a pré-deformação e a recarga foi analisada através observações por microscopia electrónica de transmissão, difracção de raios x e simulações numéricas utilizando o modelo policristalino viscoplástico auto-consistente.

Os resultados obtidos mostraram que a liga AZ31 apresentava um comportamento mecânico durante a recarga fortemente anisotrópico, caracterizado por uma diminuição da tensão de escoamento com o ângulo entre as duas trajectórias de deformação. De acordo com os cálculos realizados, este comportamento está associado a uma diminuição do valor médio do factor de Taylor devido ao desenvolvimento de uma textura cristalográfica do tipo (0001)$< 10\bar{1}0 >$ durante a pré-deformação.

keywords

Magnesium alloy AZ31, plastic anisotropy, dislocation structure,crystallographic texture, viscoplastic self-consistente model.

abstract

In this work, the effect of the strain path change on the mechanical behavior of magnesium alloy AZ31 was investigated by sequential uniaxial tensile tests performed at room temperature.

The pre-strain was carried out up to a value of 0.07 in the rolling direction (RD) of the sheet. From the pre-deformed samples, specimens at 0º, 15º, 30º, 45º, 60º, 75º and 90º from the RD were cut and reload in uniaxial tensile test.

The influence of the dislocation microstructure and the crystallographic texture developed during the plastic deformation on the mechanical behavior of the material during the prestrain and reloading was analyzed by transmission electron microscopy, x-ray diffraction and numerical simulations using the polycrystalline viscoplastic self-consistent model.

The results showed that the AZ31 alloy presented a strong mechanical anisotropic behavior during reloading, characterized by a decrease of the flow stress with the angle between the two deformation paths. According to the calculations, this behavior is associated with a decrease of the average Taylor factor due to the development of a (0001)$< 10\bar{1}0 >$ type crystallographic texture during the pre-strain.

Contents

List of Tables

List of Figures

Symbols and Abbreviations

b - Burger Vector;

E – Average strain (self-consistent model);

l, l_0 – Final and initial length;

L^H - Hill's constraint tensor;

m – Schimd's factor;

<M> - Average Taylor factor;

R – Anisotropic Coefficient/ Lankford Parameter;

$\bar{R}$ & ΔR – Normal anisotropic coefficient & planar anisotropic coefficient;

t, t_0 – Final and initial thickness;

w, w_0 – Final and initial width;

W_{int} – Internal plastic work;

α – Parameter characterizing the change in the strain path amplitude;

α´ – Average interaction intensity between dislocations;

γ – Shear strain;

ε – True strain;

ε_{11} – True strain in length direction;

ε_{22} – True strain in width direction;

ε_{33} – True strain in thickness direction;

ε_p – Tensor of prestrain;

ε_r – Tensor of reloading;

η – Reciprocal strain rate sensitivity coefficient;

θ – Reloading angle;

λ –Angle between directions of applied stress and slip direction;

μ – Shear modulus;

ρ – Dislocation density;

σ – True stress;

σ_o – Yield stress;

σ_{max} – Maximum stress;

Σ – Average stress (self-consistent model);

τ_o – Friction stress for dislocation movement;

$\tilde{\tau}_c$ – Critical resolved shear stress;

τ^s – Magnitude of shear stress in the slip systems;

ϕ – Angle between directions of applied stress and normal to the slip plane;

ϕ_1,Φ, ϕ_2– Euler's angles (definition of Bunge);

ASTM – American Society for Testing and Materials;

CRSS – Critically resolved shear stress;

HB – Brinell hardness;

HCP – Hexagonal closed packed;

ND – Normal direction;

RD – Rolling direction;

SEM – Scanning electron microscopy;

TA – Tensile axis ;

TD – Transverse direction ;

TEM – Trasmission electron microscopy ;

VPSC – Visco-plastic self-consistent model

1 Introduction

Lightweight materials have an increased importance in many industrial technologies, ranging from automobile, aerospace, building, sports and medical devices. Due to its good properties, such as low density and high specific strength, magnesium alloys are in the last years emerging as a strong candidate to replace other heavier materials like, for example, steel and even aluminium.

Most of the industrial metals forming processes involve a complex deformation history, during which the material is subjected to successive strain paths that may vary considerably in their orientation. These changes in strain path have a relevant effect on the mechanical behavior of metals. Macroscopically the effect of a prestrain becomes manifested by a change of work hardening rate as, for example, an increased reloading yield stress, temporary hardening and/or softening that can lead to premature failure. For that, investigation on the effect of change of strain path on the mechanical behavior of the Mg alloys is of vital importance.

The plastic deformation and mechanical behavior of Mg and its alloys are found to be dependent on various factors i.e. the orientation of the grains (crystallographic texture), the deformation conditions (i.e. the temperature, strain rate, strain path) (Mohd Ruzi, 2009). However, previous studies on wrought Mg alloys were concentrated on the effect of temperature and strain rate upon the mechanical behavior (Mohd Ruzi, 2009). On the other hand, research on the effect of change of strain path on the mechanical behavior of material was found to be less investigated.

Hence, the present study aims at to the determination of the influence of change of strain path on the mechanical behavior at room temperature of a Mg alloy. The evolution of dislocation structure and the crystallographic texture and its contribution to the observed behavior was also under concern.

The present thesis is organized in the following way:

In the chapter 2 a bibliographic review is presented, where the main properties and applications of magnesium alloys are given to. This chapter also covers the main aspects of

plastic deformation, crystal texture and their influence on the mechanical properties of metals.

Chapter 3 describes the initial material, experimental work and used techniques for the material characterization.

The chapter 4 describes the results and their discussion.

The conclusions and proposals for future work are presented in short chapters 5 and 6, respectively.

2 Literature review

2.1 Magnesium and its alloys

Magnesium is the seventh most abundant element in the Earth's crust where it comprises about 2% per mass. It is one of the lightest metals that are currently used as structural metallic materials. During many years Mg was used mostly in its compound forms and it was very recent undertaking to use Mg and its alloys in structural applications. Important physical properties of Mg are compared with the properties of other structural metals in Table 2.1. It can be seen that Mg has substantially lower density than Al and Fe. The values of hardness and tensile strength of Mg are higher than those of Al but the ductility is lower. The reduced ductility of Mg was (and still is) a major problem that limited the industrial applications of this metal and its alloys. Indeed, it is well known that polycrystalline pure Mg and Mg alloys exhibit low ductility and formability at room temperature. This behavior is due to hexagonal closed packed structure of this material and the limited number of operative slip systems at room temperature (Choi S. D., 2009) (Wang Y. H., 2003) (Engler, 2010).

In most of industrial applications, the magnesium is used in alloyed form. In fact, alloying is one of the most important way to improve strength, creep resistance, heat resistance etc. of the material. For instance, alloying Mg with Al provides solid solution strengthening. Contemporarily, Al is the most used alloying element in Mg and if given in amounts above 6% provides age hardening by the formation of the $Mg_{17}Al_{12}$ phase (fig. 2.1). Addition of Zn helps to improve castability and corrosion resistance of Mg alloys.

Magnesium alloys are classified according to the way they have been processed. Cast (die & sand) and wrought are the typical end products of different processing routes of Mg and its alloys (fig. 2.2). Each of the processing routes has been tailored to give emphasis on an individual property. As a result, several different alloys exhibiting different properties have been developed over the years. The commercially most used Mg alloys include the AZ series (Mg-Al-Zn), AM series (Mg-Al-Mn), AE series (Mg-Al-RE), EZ series (Mg-RE-Zn) ZK series (Mg-Zn-Zr) and WE series (Mg-RE-Zr) (Cahn, 1999).

Table 2.1 *- Some physical property exhibited by Mg, Al and Fe (Watarai, 2005)*

Metal	Specific gravity (g/cm^3)	Melting point (^oC)	Boiling point (^oC)	Latent heat of melting (J/cm^3)	Specific heat ($J/cm^3.K$)	Coefficient of thermal expansion $\times 10^6$ (K^{-1})	Tensile strength (MPa)	Elongation (%)	Hardness HB
Mg	1.74	650	1110	640	1.84	25.5	98	5	30
Al	2.74	660	2486	1088	2.43	23.9	88	45	23
Fe	7.86	1535	2754	213	3.68	11.7	265	45	67

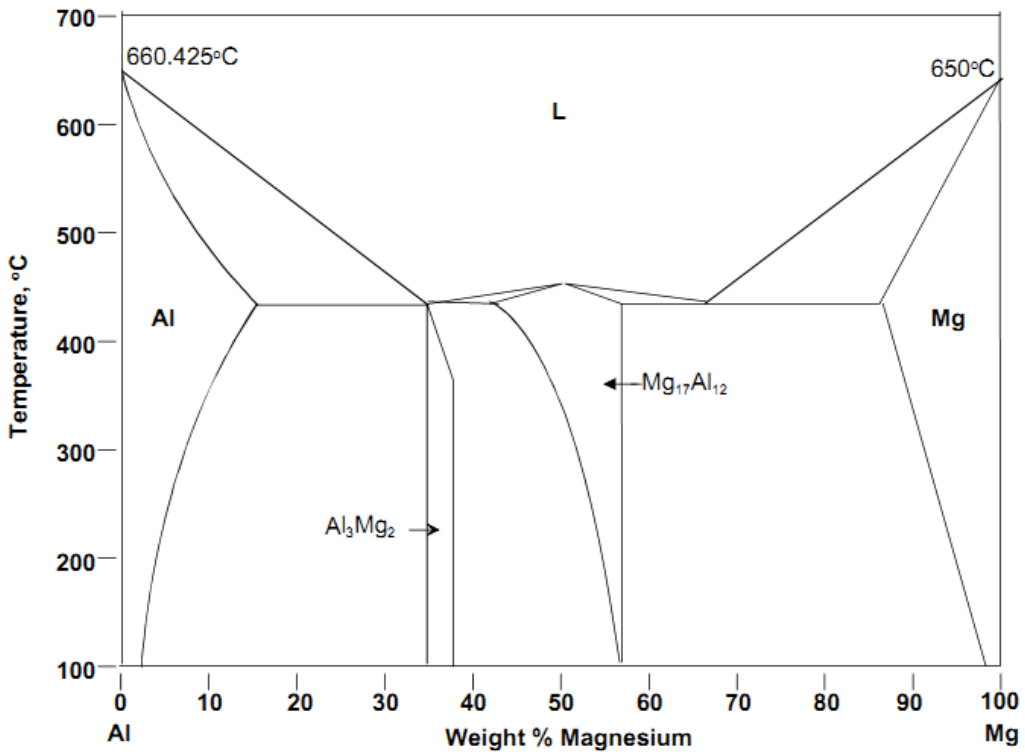

Figure 2.1 *- Mg-Al phase diagram (Wei, 2006)*

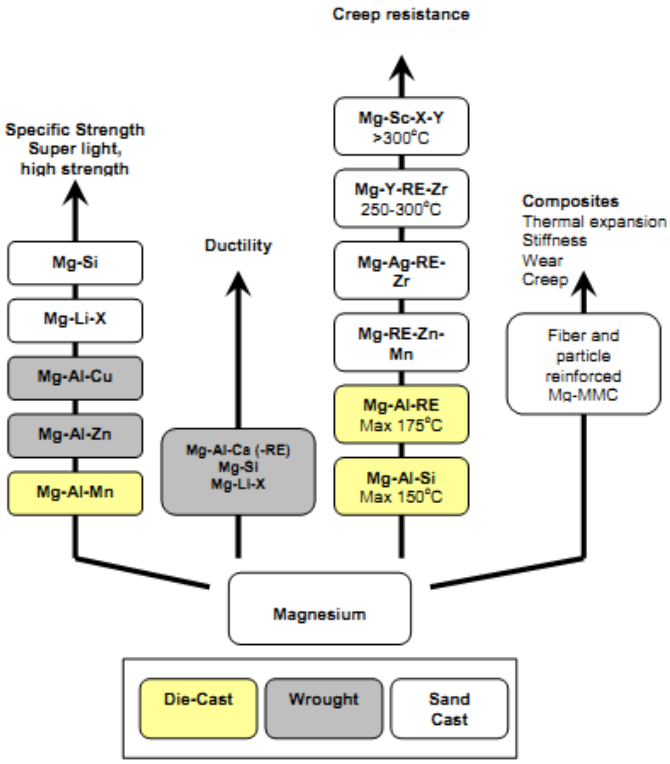

Figure 2.2 *- Classification of Mg alloys (Avedesian, 1999)*

Mg and its alloys are mainly used in marine, electronics, aerospace and automotive industries (Mordike, 2001). In these last industries there are several important requirements that influence the selection of the material, such as safety, weight, mechanical properties etc. (fig. 2.3). Global trends to produce light weight, environmentally friendly, safer and cheaper vehicles are more of recent demand (Friedrich H. S., 2001) (Alan, 2003) (Schumann, 2003) which has led the way to enormous prospective of Mg and its alloys. Nowadays, the largest automobile manufacturers are trying to reduce the vehicle weight in order to significantly decrease energy consumption (Cole, 2007) (Gerald, 2003). Since the vehicle weight is directly related to the fuel economy as well as CO_2 emission (fig. 2.4), reducing it has been a major issue.

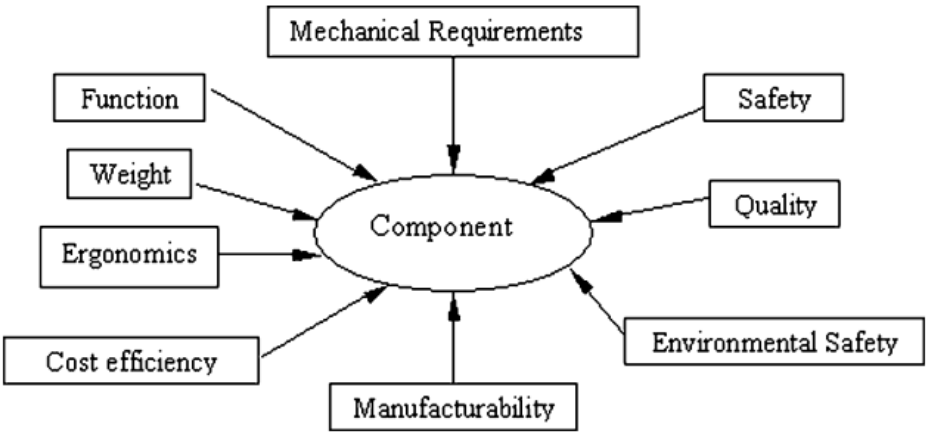

Figure 2.3 *- Component requirements of vehicles (Davies, 2003)*

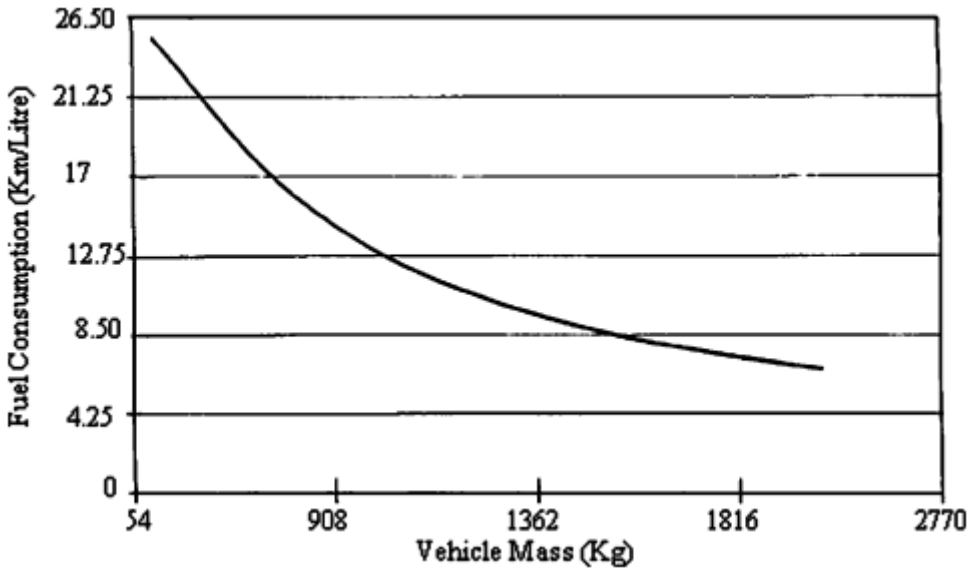

Figure 2.4 *-The relation between the fuel consumption and vehicle mass of automobiles (Eliezer, 1998)*

Some major applications of magnesium and its alloys in automotive industry are in body parts where stiffness, surface quality, corrosion resistance and formability issues needs to be taken care of, engine and transmission components where stiffness, resistance to heat, corrosion resistance have to optimized, interior parts like seat, steering parts, the chassis parts like wheels, suspension arms etc. Other structural uses of magnesium and its alloys were in aircraft fuselages, engine parts, and wheels. They are now also used in jet-engine parts, rockets, luggage frames, portable power tools, cameras and optical

instruments. Another important use of Mg alloys is in anodic protection of the corrosion of iron and steel, as in pipelines and ship bottoms. For this purpose a magnesium plate is connected electrically to the iron. The rapid oxidation of the magnesium prevents the oxidation and corrosion of the iron. A pie chart for typical commercial usage of Mg is presented below (fig. 2.5).

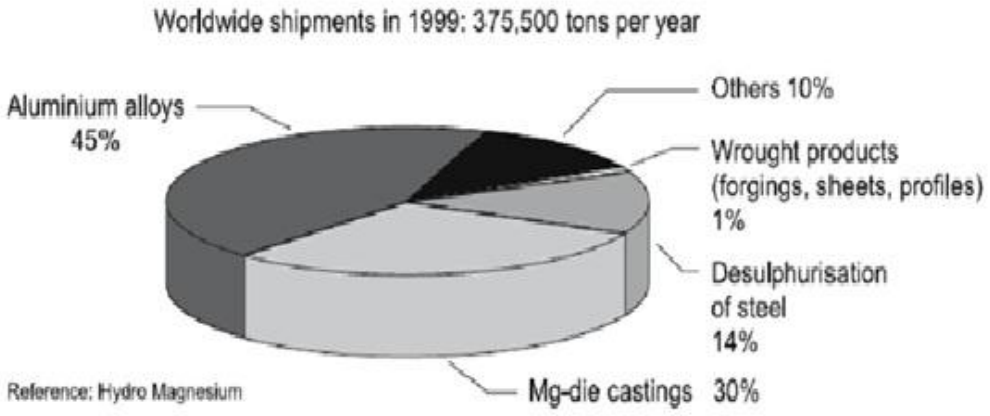

Figure 2.5 - *Main fields of magnesium application (Friedrich H. E., 2006)*

2.1.1 Wrought Mg alloys

Nowadays wrought Mg alloys are gaining remarkable technological importance. Over the past few years the research was more intense on wrought Mg alloys than to the cast Mg alloys.

Cast Mg products are typically known to possess structural defects, pores and segregation which lead to their low strength, ductility and creep resistance (Lee S.-H. C.-Y., 2002). The process of casting also leads to wastage of material. Wrought Mg alloys, on the other hand, offers outstanding stiffness, buckling resistance as well as good dimensional stability in sheet form (Emley, 1966) (Luo, 2007) and that is why wrought Mg alloys are finding more importance in industrial applications. AZ31, AZ61, AZ80, ZK60, M1A, HK31,

HM21, ZE41, ZC71 are the members of the wrought Mg alloy group. Among them AZ31 was the most used and investigated alloy in terms of industrial applications in recent years.

Wrought Mg alloys are mainly used as extruded bars, sections, tubes, forging and rolled sheet with the operating temperature of about 220°C (Mohd Ruzi, 2009). This high temperature is used in order to increase the formability of the material through the increase in the number of slip systems available to accommodate the plastic deformation. Light weight, good high temperature mechanical properties and excellent corrosion resistance has led to an increasing use of wrought Mg alloys in aerospace and automotive industries such as gearbox, intermediate compressors, generators, transmissions, engine component etc. (Duffy, 1996). Table 2.2 summarizes some important wrought magnesium alloys and their applications.

Table 2.2 *- Important wrought magnesium alloys and their applications (Davies, 2003) (Kuo, 2006) (Friedrich, 2001) (Pekguleryuz M. A., 2003) (Pekguleryuz M. E., 2003)*

Alloy designation	Alloying additives	Uses	Basic properties and applications
AZ91	9.0% Al, 0.7%Zn 0.13%Mn	General casting alloy	Good castability, good mechanical properties at T<150°C
AM60	6.0% Al, 0.15%Mn	High pressure die-casting alloy	Greater toughness and ductility than AZ91, slightly lower strength. Often preferred for automotive structural applications
AM 50	Mg-Al system	General casting alloy	Good strength, ductility, energy absorption properties and castability
AE44	Mg-Al-rare earth system	General casting alloy	Better creep behaviour and castability than AE42
AE42	Mg-4 atomic percent Al-2 atomic percent rare earths	General casting alloy	Low castability, good creep behaviour
AS41	4.2%Al, 1.0%Si	General casting alloy	Better creep resistance than AZ91 at elevated temperatures but lower strength
ZE41	4.2%Zn, 1.2%RE, 0.7% Zr	Specialist casting alloy	Rare earth addition improves creep strength at elevated temperatures. Pressure tight.
AZ31	3.0% Al, 1.0Zn, 0.2% Mn	Wrought magnesium products	Good extrusion alloy
AM20	Mg-Al system	Casting alloy	High ductility, toughness, poor die-castability
MRI 153M	Mg-Al-Ca-Sr System	Casting alloy	For high temperature applications up to 150°
MRI 230D	Mg-Al-Ca-Sr System	Casting alloy	For high temperature applications up to190°
AS 21	Mg-Al-Si system	Casting alloy	For use at temperatures in excess of 120°C
AJ62	Mg-Al-Sr system	High pressure die-casting (HPDC)	Good thermal and mechanical strength, superior castability, corrosion resistance and creep behaviour

2.2 Plastic Deformation of Metals

2.2.1 Plastic deformation mechanisms

The plastic deformation (i.e. the permanent deformation) of most metals at room temperature occurs by non-diffusive mechanisms such as slip and twinning. In metals with high stacking fault energy slip is the dominant deformation mechanism whereas in metals with low stacking fault energy twinning plays the major role (Karaman, 2000).

Slip occurs by movement of dislocations along planes and directions with highest density of atoms (slip planes and slip directions) by the action of an applied shear stress. For a single crystal, the shear stress (τ^s) resolved in the particular slip plane in the slip direction (defining the slip system s) is given by:

$$\tau^s = \sigma^s \cos(\phi^s)\cos(\lambda^s) \quad (2.1)$$

Where σ is the applied stress, ϕ is the angle between the applied stress (σ) directions and normal to the slip plane, λ is the angle between the slip direction and the applied stress direction (fig. 2.6). The product of cos(ϕ^s) cos (λ^s) is called the Schmid factor (m) of the slip system thereby leading to the following equation

$$\tau^s = m^s \sigma^s \quad (2.2)$$

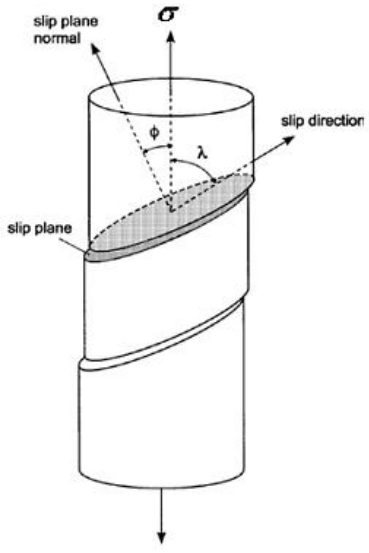

Figure 2.6 *- Slip in a single crystal (Dieter, 1988)*

The Schmid law states that the slip on a slip system and thereby the plastic deformation of the single crystal will occur if the shear stress applied (τ^s) is equal to a critical value (τ_c). i.e.

$$\begin{cases} \tau^s = \tau_c^s - slip\ \ system\ \ s\ is\ \ active \\ \tau^s < \tau_c^s - slip\ \ sytem\ \ s\ is\ \ latent \end{cases}$$

The value of τ_c depends on the friction stress for dislocation movement (τ_o) and the dislocation density (ρ) through the equation:

$$\tau_c = \tau_o + \alpha' \mu b \sqrt{\rho} \qquad (2.3)$$

Where α' is the average interaction intensity between dislocations, μ is the shear modulus and b is the magnitude of Burgers vector of the dislocations.

Twinning, on the other hand, is a unidirectional deformation mode characterized by a reorientation of the crystal lattice while keeping the crystal structure unaltered (fig. 2.7). The term mechanical twinning is defined by the activation of twinning during mechanical loading. The twin planes separate the twinned region from the untwinnied one.

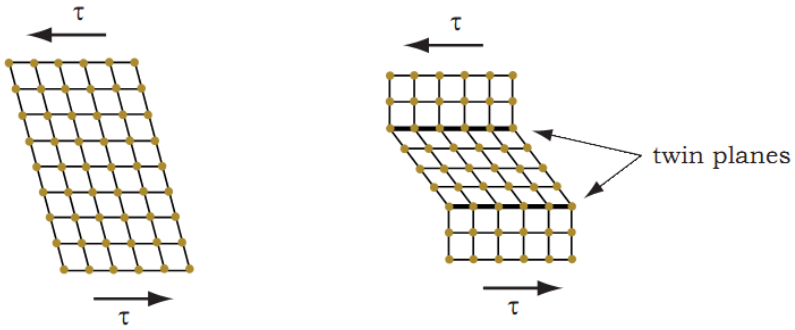

***Figure 2.7** - Mechanical twinning and crystal deformation (Graff, 2008)*

2.2.1.1 Dislocation structure

During the plastic deformation dislocations are accommodated inside the grains and, after certain amount of strain, tend to organize themselves into structures, defining dislocation cells where their shape depends on the number of activated slip systems. Namely, when one or two slip systems are activated one or two families of dislocation walls parallel to the traces of the slip planes with highest activity are developed. When more than two slip systems are preferentially activated, equiaxial cells are observed (fig. 2.8). With the increase of the applied strain, the density of accumulated dislocations increase, the size of dislocation cells decrease and crystallographic misorientations between neighbor cells increase. However, the organization degree of the dislocations depends on their mobility. Indeed, well defined intra-granular dislocation structures can be observed in materials with low friction stress for dislocation movement (τ_o) i.e. with low lattice friction, low solute and precipitate content, high stacking fault energy, easy cross-slip and climb of dislocations. By contrast, materials with high friction stress for dislocation movement tend to present a homogeneous distribution of dislocations and no cells are defined inside the grains (Rauch, 2004).

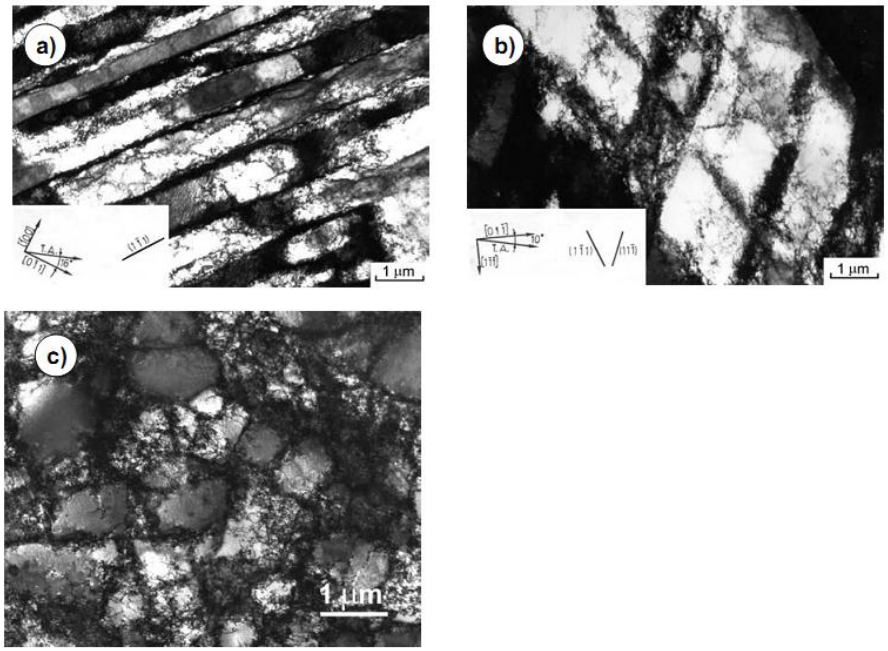

Figure 2.8 *- TEM dislocation microstructure of a) one and b) two families of parallel dislocation walls, c) equiaxial dislocation cells (Lopes A. L., 2001)*

2.2.1.2 Plastic deformation of Mg and its alloys

Although Mg is renowned as one of the most abundant metal in the Earth it did not find considerable usage in industry. As mentioned before, the most important reason for Mg and its alloys to have limited industrial applications is poor formability at room temperature. This is due to a reduced number of slip systems available to accommodate the plastic deformation in the hexagonal closed packed (HCP) structure of Mg. At higher temperature, additional slip systems become active providing greater freedom for the deformation to occur.

Mg can deform both by slip and twinning. The deformation modes are the slip on basal <a> planes ($\{0001\}\langle 11\bar{2}0\rangle$), pyramidal <a> slip ($\{10\bar{1}1\}\langle 11\bar{2}0\rangle$), prismatic <a> slip ($\{10\bar{1}0\}\langle 11\bar{2}0\rangle$) and pyramidal <c+a> slip ($\{11\bar{2}2\}\langle 11\bar{2}3\rangle$) (Proust, 2009) (table 2.3 and fig. 2.9). At room temperature, the basal slip is the dominant deformation mechanism of Mg (Proust, 2009) (Wang Y. H., 2003) (Choi S. D., 2009) (Choi S. E., 2007) (Al-Samman, 2008) (Barnett, 2009) (Koike, 2005). However, the activation of this slip system does not allow the deformation of the crystal along the c-axis since it is perpendicular to this axis. To accommodate the plastic deformation along the c-axis other crystallographic directions (i.e. the <c+a> directions) needs to be activated. Deformation in the c-axis direction can occur either by twinning or slip, mostly depending on the temperature (Staroselsky A. , 2003) (Yoo, 2002). Twinning has been attributed to play the dominant role at room temperature. At higher temperature pyramidal <c+a> slip is found to be responsible for deformation in the c-axis direction (Staroselsky A. , 2003). In particular, for AZ31 alloys basal slip was found to be dominant at temperatures up to 225^{o}C. The activation of non-basal slip systems at higher temperatures were found to be dependent on the crystallographic texture developed during thermo-mechanical processes (Yi S. , 2005).

Table 2.3 *- Slip in Mg materials (Wang Y. H., 2003)*

Slip type	Slip plane	Slip direction	Number of non-parallel planes	Slip direction per plane	Number of geometrical slip systems	Number of independent slip systems
Basal	{0001}	$<11\bar{2}0>$	1	3	3	2
Prismatic <a>	$\{10\bar{1}0\}$	$<11\bar{2}0>$	3	1	3	2
Pyramidal <a>	$\{10\bar{1}1\}$	$<11\bar{2}0>$	6	1	6	4
Pyramidal <c+a>	$\{11\bar{2}2\}$	$<11\bar{2}3>$	6	1	6	5

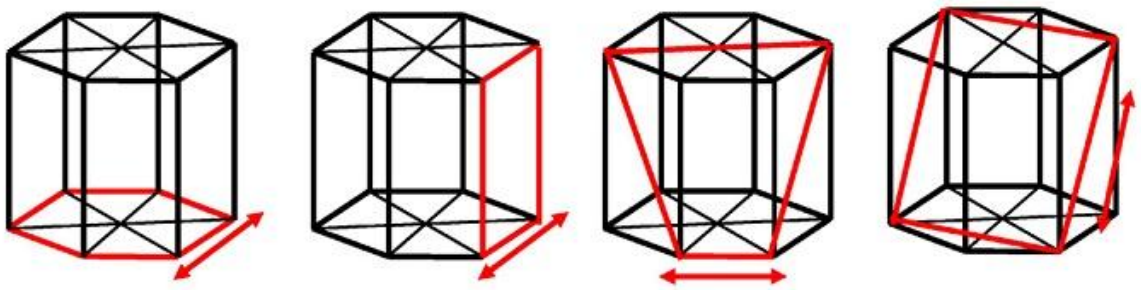

Figure 2.9 *- Slip systems in HCP materials (Choi S. E., 2007)*

Mg and its alloys generally offer two different kinds of twinning modes i.e. tensile ($\{10\bar{1}2\}<\bar{1}011>$) and compression twinning ($\{10\bar{1}1\}<10\bar{1}2>$) (Choi S. E., 2007) (fig. 2.10). The deformation twins interact in a complex manner with slip changing the mechanical behavior and texture evolution of the material. This last effect is evidenced by the strong changes of texture promoted by the reorientation of c-axis of the grains by 86.6^{o} due to the activation of tensile twins (Proust, 2009).

The activation of twinning depends on the c/a ratio of the crystal lattice. When the axial ratio (c/a) is less than 1.73 the tensile twinning can be activated by imposing a tensile stress parallel to the c-axis (Gehrmann, 2005) (Brown, 2005) (Emley, 1966). If the tensile stresses are parallel to the basal plane, compression twinning occurs. However, in this case, the activation twinning requires high stress and/or favorable dislocation structures for nucleation to occur (Barnett M. N., 2009). Twinning can contribute to primary creep

(Emley, 1966) and can also be activated both in hot and cold rolled magnesium alloys. Some studies identified twinning as the prominent deformation mode in rolled AZ31 alloys and can also be observed after tensile test (Hartig, 2005) (Kim, 2005). The amount of shear associated with the twinned grains is reported to be dependent on the axial ratio and the composition of the alloy (Staroselsky A. , 2003).

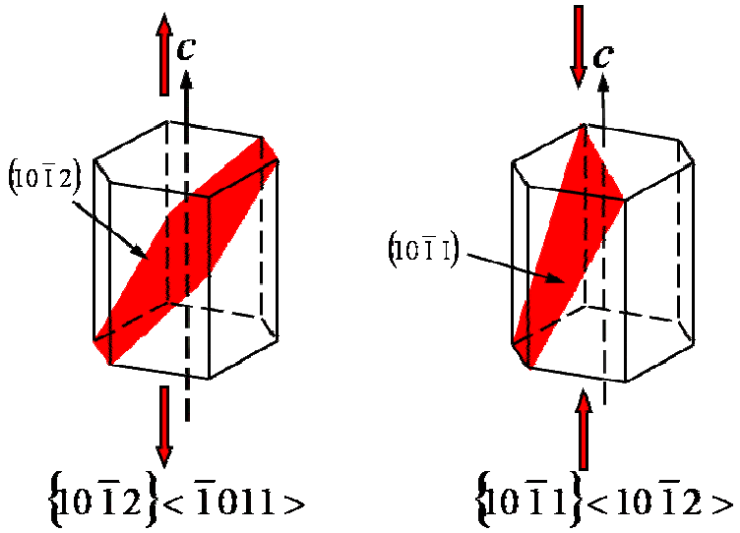

Figure 2.10 *- Tensile and compression twinning (Choi S. E., 2007)*

2.2.2 Polycrystalline models of plastic deformation

Polycrystalline materials consist of several crystallites that are usually oriented in different directions. As there are several grains in the polycrystalline material, mutual interactions among the grains occur during the deformation. Thus each grain of the polycrystal cannot deform freely as a monocrystal due to the applied stress. Mutual interaction during the deformation of the grains leads to an additional local stresses that have to be accommodated and to a differences between the microscopic and macroscopic imposed strain/stress states. Different models have been proposed to correlate the mechanical behavior of polycrystalline materials and their single crystals. Some of these models are presented during this section.

2.2.2.1 Sachs Model

The Sachs model (Sachs, 1928) presumes that the interaction stresses between neighboring grains are null. Therefore, the model considers that, the stress imposed upon each grain is uniform and equal to the macroscopic stress. In order to accommodate stress, deformation will take place by activation of the slip systems with the largest Schmid factor (eqn. 2.1). The stress applied to the crystal should attain the critical resolved shear stress (CRSS) for deformation to occur.

The entire behavior of the polycrystal can, therefore, be represented by the weighted average behavior of the individual crystal (Zaoui, 1990).

$$\sigma = < M^{-1} > \tilde{\boldsymbol{\tau}} \qquad (2.4)$$

Here, $< M^{-1} >$ is the mean value of the inverse Taylor factor and $\tilde{\boldsymbol{\tau}}$ is the average shear stress acting on the crystallites.

2.2.2.2 Taylor Model

The Taylor model states that, all of the crystallites suffer the same plastic deformation that has been macroscopically imposed on the entire material (fig. 2.11). The Von Mise's yield criterion states that the condition for homogeneous deformation requires activation of at least five independent slip systems in each grain. The slip systems that are being activated for the homogeneous deformation are not arbitrary. The model assumes that, the activated slip systems are the ones that minimize the internal plastic work. This condition can be represented by the expression below (Taylor, 1938).

$$\left(W_{\text{int}}\right)_{\min} = \left(\sum_{s=1}^{5} \tau_0^s \left| \gamma^s \right| \right)_{\min} \qquad (2.5)$$

where, $(W_{int})_{min}$ represents the minimum internal work that is necessary to plastically deform the polycrystalline material, the τ_o^s and γ^s represents the critical resolved shear stress and the shear stress in the slip system 's', respectively.

This condition can occur for different sets of five independent slip systems, giving rise to ambiguity in the selection of the activated slip system that limits the application of this model.

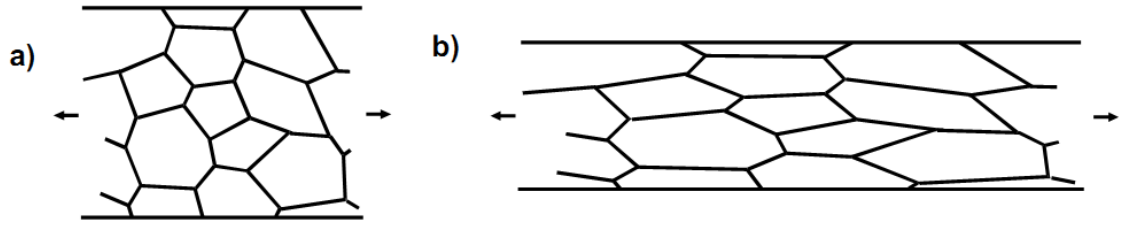

Figure 2.11 *- Taylor model prediction of the deformed grain [Schematic] a) Initial Condition, b) after deformation (Lopes A. L., 2001)*

From the macroscopic and microscopic energy conservation law (Kocks, 1970)

$$\sum_{i,j=1}^{3} \sigma_{i,j}\varepsilon_{i,j} = \left(\sum_{s=1}^{S} \tau_c^s \left| \gamma^s \right| \right)_{\min} \qquad (2.6)$$

Admitting that the critical shear stress value is the same for all slip systems ($\tau = \tau_c^s$)

$$\frac{\sigma}{\tau} = \frac{\left(\sum_{s=1}^{S} \left| \gamma^s \right| \right)_{\min}}{\varepsilon} = M \qquad (2.7)$$

where, the σ and ε are the macroscopic imposed stress and strain. M is the Taylor factor which is a parameter that takes into account the orientation of the grains with respect to the applied stress. If all the grains are taken in account, the Taylor factor (M) should be replaced by the average Taylor factor (<M>) and the previous expression can be rewritten as:

$$\sigma = \langle M \rangle \tilde{\boldsymbol{\tau}} \qquad (2.8)$$

2.2.2.3 Self-consistent Model

Self-consistent model considers the grains as an inclusion in a fictitious homogeneous medium where the property of the entire matrix depends on the weighted average of the individual grain contribution, taking into account its crystallographic orientation (Kocks, 1998).

$$E = \langle \varepsilon \rangle \tag{2.9}$$

and,

$$\Sigma = \langle \sigma \rangle \tag{2.10}$$

where, the $\langle \varepsilon \rangle$ and the $\langle \sigma \rangle$ represent the average strain and average stress and E and Σ represent the macroscopic stress and strain, respectively.

One of the most successful equations that relate the above mentioned parameters was proposed by Hill (Hill, 1965).

$$\sigma - \Sigma = - L^{H} (\varepsilon - E) \tag{2.11}$$

Here the L^{H} is the Hill's constraint tensor, which depends on the grain shape and the grain orientations.

2.2.2.4 Visco-plastic Model

In the visco-plastic model the shear strain rates ($\dot{\gamma}^{s}$) in each slip system is related with the resolved shear stress (τ^{s}) by a continuous and non-linear power law expression (Molinari, 1987).

$$\dot{\gamma}^{s} = \dot{\gamma}_{c}^{s} \left(\frac{\tau^{s}}{\tau_{c}^{s}} \right)^{\eta} \tag{2.12}$$

In the above equation, the $\dot{\gamma}^{s}$ and the τ_{c}^{s} are, respectively, the reference shear strain rate and the critical resolved shear stress (CRSS) of the slip system s. The η is the reciprocal strain rate sensitivity coefficient of the material.

This model assumes that all slip systems are activated (but with different activity) during the plastic deformation, removing Taylor's model ambiguity in the selection of the activated slip systems (Lopes, 2001).

2.2.3 Crystallographic Texture

Crystallographic texture is defined as the preferred orientation of the grains with respect to a macroscopic reference frame defined in the sample. In the case of rolled metals the axes of the external reference frame are commonly defined by the rolling direction (RD), transverse direction (TD) and normal direction (ND) (fig 2.12).

This preferential orientation of the grains imposes anisotropy of properties (for example, the strength, electrical conductivity, piezoelectricity, magnetic susceptibility, light refraction, wave propagation etc.) and can be modified both by plastic deformation and heat treatment processes.

Crystallographic texture can be represented by different methods. Of them, pole figures are the most widely used techniques where the crystallographic plane normal density is represented through stereographic projections. One pole figure alone is not sufficient to completely define the orientation of the crystallites and it is necessary to measure the pole figures for at least two different crystallographic planes.

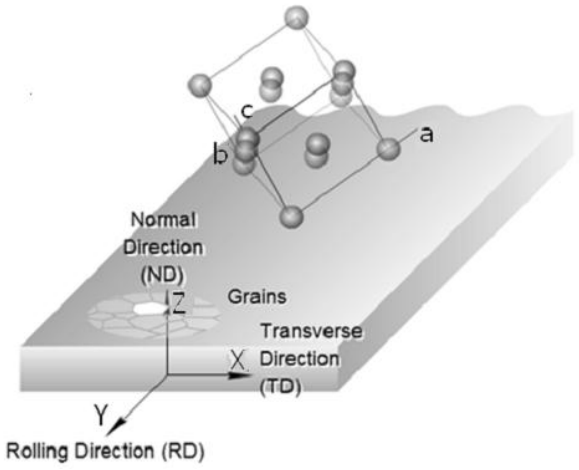

Figure 2.12 - *Definition of crystal axis (a, b, c) and macroscopic specimen axis (X, Y, Z) (Aluminium Matter, 2011)*

In the case of sheets, the preferential crystallographic orientation of the grains can also be identified by the {hkl} plane and <uvw> directions parallel to, respectively, the sheet plane and RD.

A more complete representation of the grain orientations in the polycrystal is by three consecutive rotations (Euler angles: ϕ_1,Φ, ϕ_2) that transform the crystal coordinate system (a,b,c) to the macroscopic sample coordinate system (X, Y, Z). Fig. 2.13 shows the sequence of operation for this transformation.

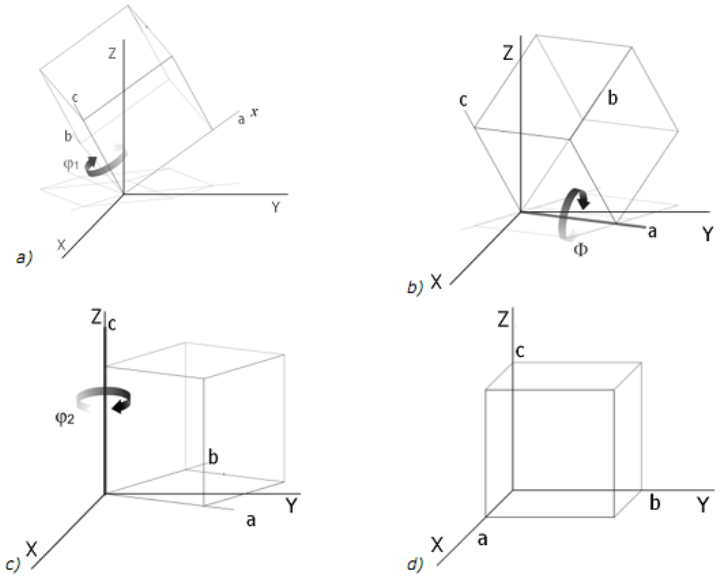

Figure 2.13 - *Euler's angle definition of Bunge showing the rotation sequence from a) to d) (Aluminium Matter, 2011)*

The Euler's angles that characterize the orientation of each crystal in the material can be represented in the Euler's (ϕ_1,Φ, ϕ_2) coordinate system (Euler's space). As a result, the orientation of each crystal in a polycrystal can be expressed as a point in the 3D space and the texture of the polycrystal can be represented by a 3D-iso surface (fig. 2.14 (a)). However, in the last case, the resulting three dimensional representation is complex and it is more common to represent the polycrystal texture by 2D sections of Euler space at constant ϕ_2 (fig. 2.14 (b)).

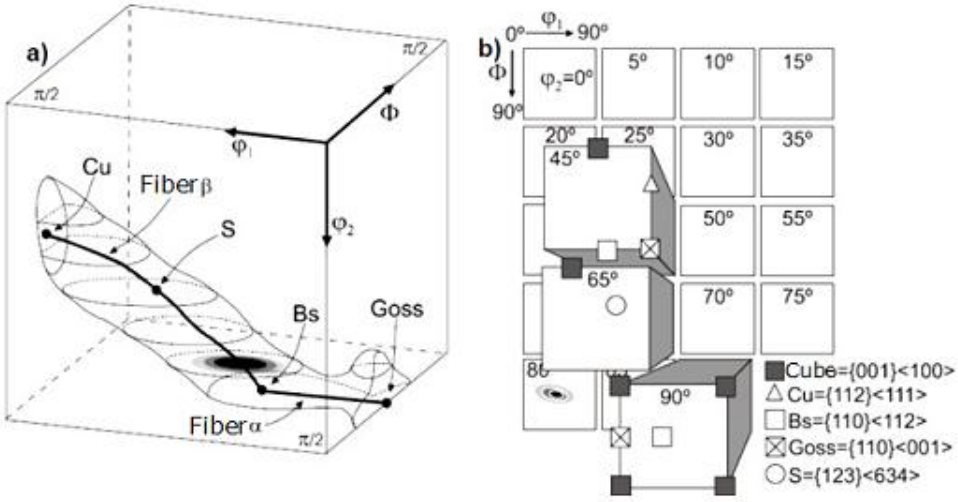

Figure 2.14 – *Crystallographic texture representation in Euler's space a) three-dimensional representation; b) two-dimensional representation of sections with constant values of φ_2 (Bunge, 1982)*

2.2.3.1 Texture in Mg and its alloys

The crystallographic texture of HCP metals has attracted significant interest because usually play an important role in many mechanical and physical properties of these materials.

The process conditions play a vital role to the development of texture (Gehrmann, 2005) (Kim, 2005) (Agnew, 2003) (Azhi, 2008). The texture affects the deformation mode which in turn promotes changes on the crystallographic orientation of the grains (Wang, 2010). Texture can develop during processing and solidification and afterwards can be modified by plastic deformation, phase transformations as well as recrystallization (Kawalla, 2007).

According with the c/a unit cell length ratio, the texture of cold rolled HCP metals can be classified in three groups (fig. 2.15). Metals with c/a ratio approximately equal to the ideal value (c/a ≈ 1.633), such as Mg (c/a = 1.624), tend to develop basal fiber textures where most of the basal planes are oriented parallel to the sheet plane and there is no preferential orientation of the prismatic or pyramidal planes (Wang Y. H., 2003). Some ideal pole figures of this group of metals are shown in figure 2.16. The dominance of slip in the basal planes during plastic deformation of Mg sheets was attributed to this kind of texture development (Wang Y. H., 2003). Metals with c/a ratio above 1.633, such as Zn (c/a ≈

1.856) and Cd (c/a ≈ 1.885), have the propensity to show texture where the basal poles are tilted ±15°–25° away from the normal direction towards the rolling direction (fig. 2.15(b)). The combination of basal slip and large scale twinning give rise to this texture (Wang Y. H., 2003). Metals with c/a ratio less than the ideal one, such as Zr (c/a ≈ 1.589) and Ti (c/a ≈ 1.587), typically show texture where the basal poles are tilted ±20°–40° away from the normal direction towards the transverse direction (fig. 2.15(c)). The activation of prismatic plane slip was made responsible for this type of texture (Wang Y. H., 2003).

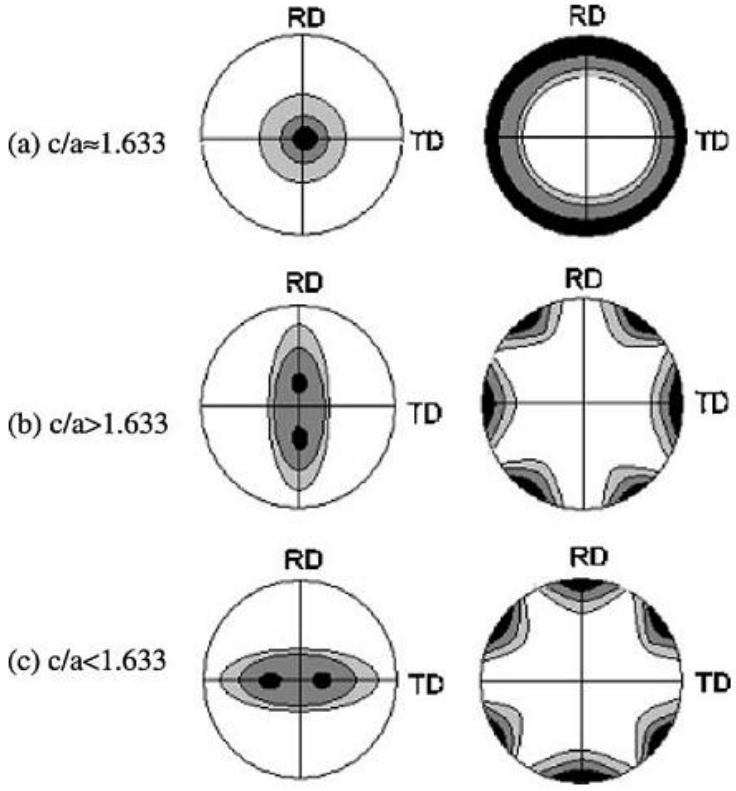

***Figure 2.15** - Simulated {0001}, {10$\bar{1}$0} rolling texture in HCP metals with c/a ratio: (a) approximately equal to 1.633; (b) >1.633; and (c) <1.633 (Wang Y. H., 2003).*

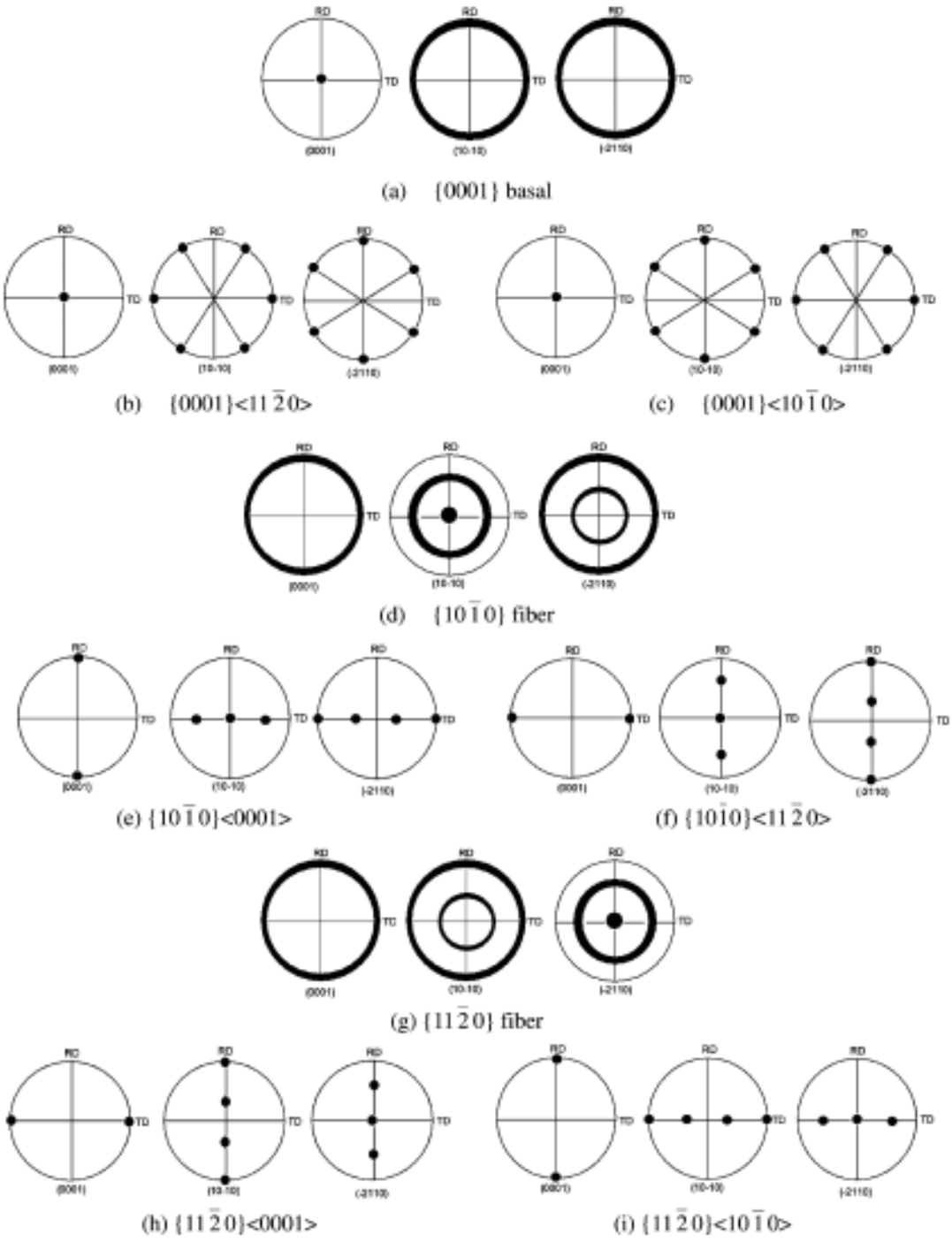

Figure 2.16 - *Some important ideal pole figures of HCP metals (Wang Y. H., 2003)*

In all the materials of the three groups, the evolution of initial texture during the deformation depends on the deformation mode and direction (Löffler, 2007). In figure 2.17 is presented an example of AZ31 rolled sheet (fig. a and b) after compression test along RD (fig. c) and tensile tests along ND (fig. d). It is noted that clear distinct textures were developed for both tests. For compression along RD the pole figures show a strong reorientation of the grains giving rise to split of basal poles along the RD direction as a result of a strong tensile twinning activity. For tension along ND the basal poles of the twinned regions were randomly orientated on the RD-TD plane (Park, 2010).

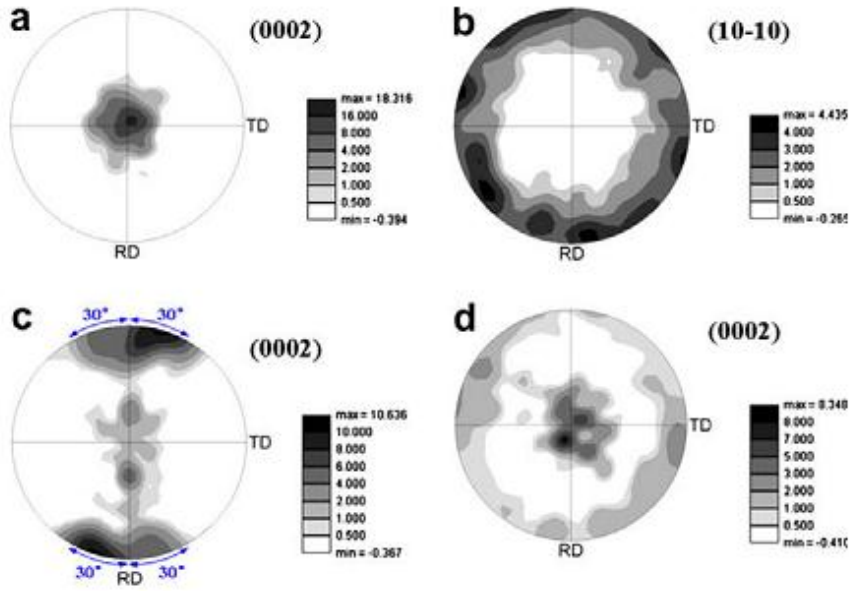

***Figure 2.17** - Pole figures: (a) (0 0 0 2) and (b) (1 0 $\bar{1}$ 0) of the as-rolled material, and (0 0 0 2) of the material (c) compressed to 6% along the RD and (d) tensioned to 6% along the ND (Park, 2010)*

2.2.4 Plastic anisotropy

Anisotropy is defined as the variation of properties (strain, stress, strain hardening etc.) along different directions. For the strain, the anisotropy can be characterized by the anisotropy coefficient, or Lankford parameter, (R) defined as the width to thickness reduction ratio:

$$R = \varepsilon_{22} / \varepsilon_{33} \quad (2.13)$$

Here ε_{22} is the true strain of the width and ε_{33} is the true strain of the thickness (fig. 2.18).

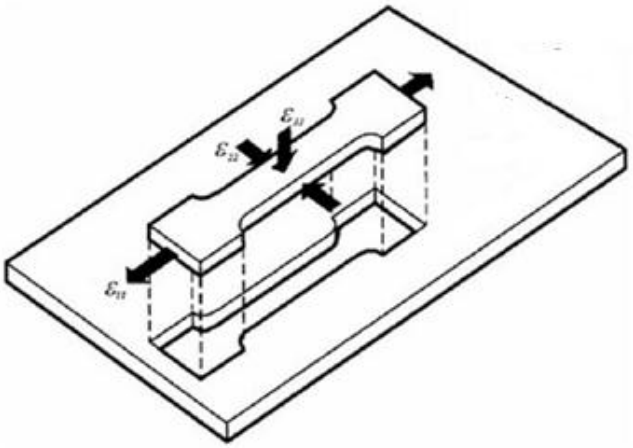

Figure 2.18 *- Definition of strain tensor components (Vincze, 2007)*

The average value and variation of R-values with the test direction are expressed by the normal anisotropy ($\overline{R}$) and planar anisotropy (ΔR) coefficients respectively (Banabic, 2000).

$\overline{R} = (R_0 + R_{90} + 2R_{45})/4$ and

$\Delta R = (R_0 + R_{90} - 2R_{45})/2 \quad (2.14)$

Where R_0, R_{45} and R_{90} are the R-values for 0^o, 45^o and 90^o from the rolling direction of the sheet.

The normal anisotropy is an important indication of the material deep drawability. Higher the value of normal anisotropy characterizes higher deep drawing ability and larger strain can be attained without rupture. The forming limit diagram (fig. 2.19) is usually deployed in order to represent the effect of anisotropy on the formability of the material. The planar anisotropy coefficient is associated with the development of earring. When $\Delta R = 0$, the deformation in sheet plane is isotropic and no earring occurs. For $\Delta R > 0$, earrings form at 0^o and 90^o directions. Where $\Delta R < 0$, earrings form at 45^o from RD.

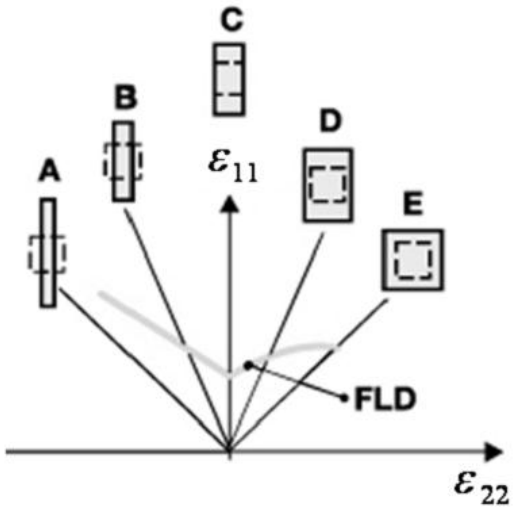

Figure 2.19 - *Forming limit diagram: A pure shear, B uniaxial tension, C plain strain, D stretch forming, E equibiaxial strain (Bahadirov, 2010)*

Anisotropy is a macroscopic effect of crystallographic texture and dislocation microstructure developed during the plastic deformation of the material. Therefore, a special attention must be paid to both of these aspects in order to control the mechanical behavior of the material during the forming processes.

2.2.4.1 Effect of crystallographic texture

For an undeformed metal, the anisotropy is determined by the initial crystallographic orientation of its grain. This effect has been reported in several works (Brown, 2005) (Choi S. D., 2009) (Gehrmann, 2005) (Styczynski, 2004). For example, in the study performed by Yi (Yi, S. B. 2006), the anisotropic mechanical behavior of the AZ31 Mg alloy was described in relation to the crystallographic texture. Specimens were taken at 0^o, 45^o and 90^o to the extrusion direction and uniaxially loaded in tension at room temperature. The results in fig. 2.20 show a strong anisotropic behavior of the material, expressed by different flow stress evolution and uniform strains. These differences were attributed to the strong initial texture of Mg bars and to the activation of different deformation modes.

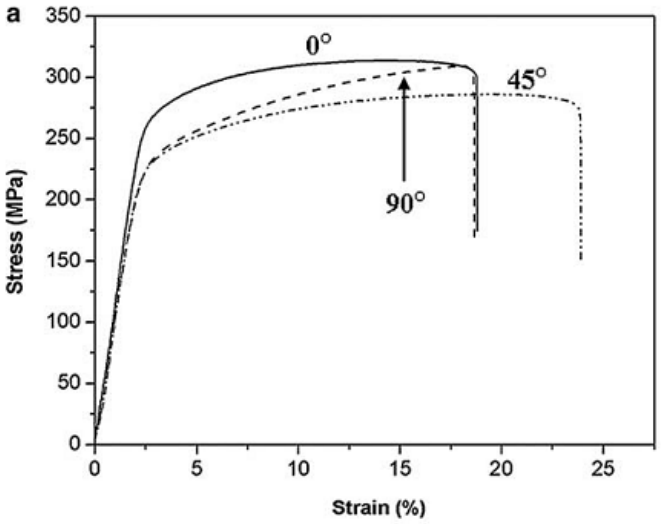

Figure 2.20 - *Flow curves during tensile test at different orientations from extruded direction of Mg bar (Yi S. C., 2006)*

2.2.4.2 Effect of dislocation microstructure

Most of the industrial metals forming processes involve a complex deformation history, during which the material is subjected to successive strain paths that may vary considerably in their orientation. These changes in strain path have a significant effect on the mechanical behavior of metals. Macroscopically the effect of a certain prestrain becomes manifested by a change of work hardening rate as, for example, an increased reloading yield stress, temporary hardening or softening. In the last case, strain localization can occur and leads to a premature failure and, therefore, to a decrease of material formability. This effect is strongly anisotropic and depends on the prestrain value.

The mechanical behavior of the prestrained material during reloading can be grouped into three different types and is represented schematically in fig. 2.21.

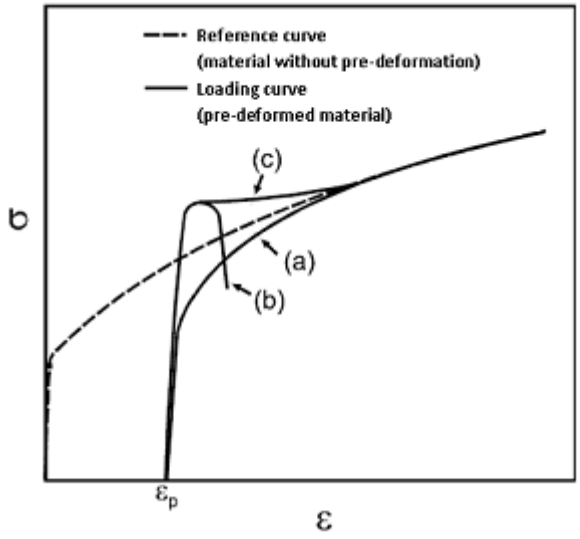

Figure 2.21 – *Stress (σ) – strain (ε) curve showing the consequences of reloading after a pre-deformation comparing with the initial monotonic test. For a) b) and c) see text. (Vieira, 1994).*

The curve (a) represents the case where the yield stress during reloading is lower than the yield stress exhibited by the undeformed material. The behavior is typical of materials when are subjected to reversal of applied load (Bauschinger test).

The curves (b) and (c) represent the situations where the yield stress during reloading shows higher values than that exhibited by the material without pre-deformation. In curve (c) the material presents similar rupture strain as undeformed material. On the other hand, curve (b) represents the situation where the material exhibit softening during the early stage of reloading that leads to its premature failure. Depending on the prestrain value and the angle between the pre-deformation and reloading, the pre-deformed material can demonstrate the behavior represented by any of the curves (a), (b) or (c).

2.2.4.2.1 Effect of prestrain value

The prestrain value influences the capability of the material to plastically deform. There exists a critical prestrain value associated with each material, after which the capability of the metal to plastically deform reduces significantly. As the value of prestrain gets higher, the material formability is reduced and subsequently fails at lower reloading strain. This

effect is due to the interaction between the dislocations activated during the reloading and the dislocation structure from pre-deformation, which is more pronounced when the material is deformed up to higher values of prestrain. In the case of mild steel the critical pre-deformation value is approximately 0.1 (Hutchinson, 1983) for second orthogonal sequence of uniaxial tension (fig. 2.22) whereas for copper the value is 0.18, for the same deformation condition (Shen, 1988).

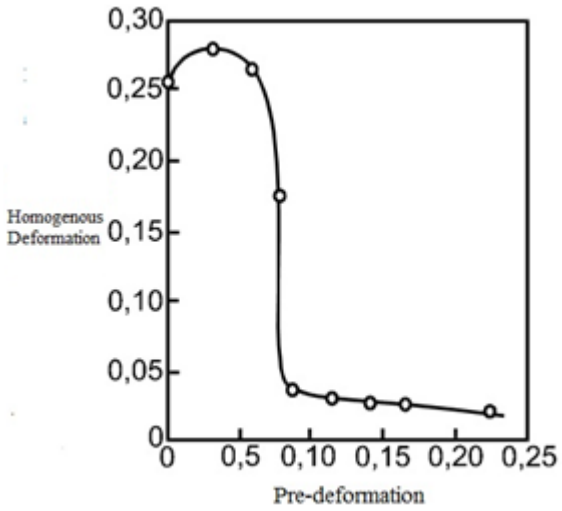

Figure 2.22 *- Effect of pre-deformation value on the homogeneous plastic deformation in mild steel deformed in second orthogonal trajectories (Shen, 1988)*

2.2.4.2.2 Effect of the amplitude of strain path change

The amplitude of the strain path change can be characterized by the parameter α defined as the cosine or the angle defined in the deformation space of the two reactions that represents the two successive deformations (Schmitt, 1994).

$$\alpha = \frac{\varepsilon_p \cdot \varepsilon_r}{\|\varepsilon_p\| \|\varepsilon_r\|} \qquad (2.15)$$

with ε_p and ε_r the tensors of prestrain and reloading, respectively.

The value of this parameter lies between 1 and -1. The value of $\alpha = 1$ corresponds to a monotonic test where the strain path has not been changed. The same slip systems are

activated in both the pre-deformation and the reloading and the mechanical behavior after reloading superimposes to the one obtained during the monotonic test.

The value of $\alpha = -1$ occurs when the strain path is reversed. In this case, the slip systems activated during the pre-deformation are reactivated in the opposite direction during reloading. As previously mentioned this test corresponds to a Bauschinger test and can be represented by the curve (a) of figure 2.21.

The value of $\alpha = 0$ corresponds to the situation where the slip systems that were latent during the pre-deformation are activated during reloading. This requires a higher flow stress to initiate the movement of dislocations in the new activated slip systems due to the low mobility of the prestrain dislocations. However, after an initial stage, the dislocation annihilation process occurs, the prestrain structure is replaced by a structure typical of the second path and the effect of the prestrain on the flow stress decreases. This give rise to a temporary softening (curve (b) and (c) in fig. 2.21) that can lead to a flow localization just in the beginning of the reloading path (curve (c) in figure 2.21.

3 Experimental Setup and Procedures

The main goal of this work is to study the effect of change of strain path on the mechanical behavior at room temperature of Mg alloy. The alloy investigated was an AZ31 wrought Mg alloy, which is the most widely used wrought Mg alloy in terms of industrial application. The as-received AZ31 alloy sheets were cut in large pieces, some of them were stored for tensile test and the remaining sheets were subjected to a two-stage interrupted tensile test (pre-straining followed by reloading) by using the uniaxial tensile machine. ASTM standard tensile specimens at different angles from the first tensile test direction were cut from the pre-strained material. Transmission electron microscopy (TEM) was conducted in order to observe the evolution of dislocation structures and twinning (if any). Afterwards, texture measurement was also conducted by using the X-ray diffraction technique. VPSC model code developed by Lebenshon and Tome (Lebensohn R. A., 1993) (Lebensohn R. A., 1994) was used to assess the effect of the orientation of the grains on the reloading behavior of the material. In the following sections, details of the important parameters (i.e. the sample dimensions, the test parameters) and equipment used are presented.

3.1 Material

In this work, the material studied was a commercial grade AZ31 alloy. The commercial grade is composed of Al (3 wt pct.), Zn (1 wt pct.) and Mg (balance). The alloy sheets were received in an annealed condition after subsequent rolling and in the form of large sheets of 3mm thickness. Typical composition of the alloy is given in table 3.1.

Table 3.1 *- Typical composition of AZ31 alloy (Gao, 2009)*

	Al	Zn	Mn	Fe	Ce	Cu	Zr	Ni
mass %	3.03	0.97	0.31	0.01	0.006	0.003	0.002	0.001

3.2 Mechanical Testing

The prestraining of the sample was carried out by cutting large test pieces (gauge length = 300 mm and width = 60mm) and then subjected to a prestrain value of $\varepsilon_p = 0.07$. The prestraining was carried out in the rolling direction (RD) in an Instron 4208 universal testing machine with a maximum load capacity of 150 KN. The cross-head speed (test speed) was 20 mm/min, which corresponds to an initial strain rate of $\dot{\varepsilon}=10^{-3}s^{-1}$. Figure 3.1 presents a view of the prestrain samples.

***Figure 3.1** - AZ31 alloy used for pre-straining*

Reloading was performed by introducing uniaxial tensile test using samples that were cut according to the ASTM standard tensile specimen of 10 mm width (fig. 3.2). The samples were made from the previously prestrained large pieces with variation of angles with respect to the rolling direction (RD).

ASTM standard tensile specimens were cut at 0^o (RD), 15^o, 30^o, 45^o, 60^o, 75^o, and 90^o (TD) from the RD (fig. 3.3). For each angle, three different samples were tested in order to validate the reproducibility of the results.

The test was performed in a Shimadzu Autograph (fig. 3.4) universal tensile machine which has a maximum load capacity of 50 kN. In order to measure the changes in the length and the width of the samples, a non-contact video extensometer MFA-25 was used.

From the load and length change data, the true stress (σ)-true strain (ε) curves (σ=f (ε)) were determined by:

$$\varepsilon = \ln\left(\frac{l}{l_0}\right) \tag{3.1}$$

$$\sigma = \frac{F}{A_0}\exp(\varepsilon) \tag{3.2}$$

Here, ε is the plastic strain, l_o and l are the initial and instantaneous length between the extensometer's grips, respectively, F is the force and A_0 the initial cross area.

Figure 3.2 *- Uniaxial Tensile Specimens(ASTM 10 mm width samples)*

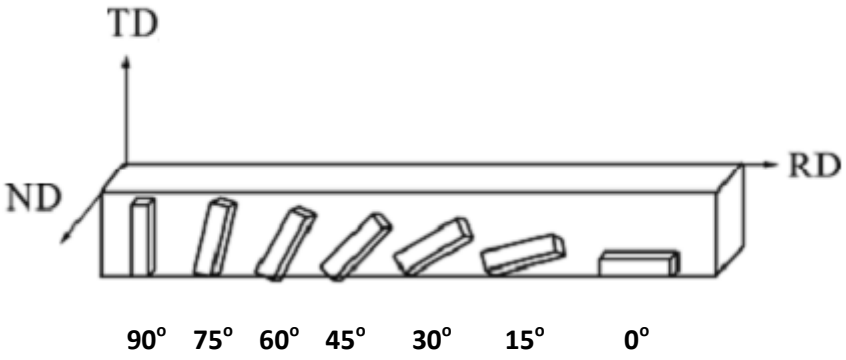

Figure 3.3 *- Sample orientations with respect to the different directions*

Figure 3.4 - *Shimadzu Autograph machine, Mechanical Engineering Department, Univ. of Aveiro*

3.3 Microscopic Observations

3.3.1 Optical Microscopy (OM)

The samples for optical microscopic observation were grinded with 180, 400, 1000, 2500 and 4000 grit SiC papers. Afterwards, they were polished using 6, 3, 1 μm diamond paste. The polished samples were etched using a standard solution of 5 ml acetic acid, 6 g picric acid, 10 ml H_2O, and 100 ml ethanol.

3.3.2 Transmission Electron Microscopy (TEM)

The dislocation structures were observed using a Hitachi H-9000 (300KV) transmission electron microscope (TEM). The TEM samples were prepared from thin foils obtained by mechanical polishing for the mid-thickness location of the sheet. The polishing was done

using 180, 400, 1000 grit SiC papers. From this thin foil, 3mm disks were cut and electropolished using a double jet thinner with a standard electrolytic solution under 10 V tension, at 20^{o}C until perforation occurred.

1 liter of electrolyte was prepared by adding and mixing 800 ml of ethanol, 100 ml of propanol and 18.5 ml of water 10 g hydroxyquinoline, 75 g citric acid, 41.5 g sodium thiocyanate, 15 ml perchloric acid.

3.4 Crystallographic texture analysis

The preferred crystallographic orientation (texture) was measured by the X-ray diffraction technique for different directions using a Philips X'pert diffractometer equipped with the texture goniometer (fig. 3.5). The diffraction intensity was measured for crystallographic planes {0002}, $\{10\bar{1}0\}$, $\{10\bar{1}1\}$ and $\{10\bar{1}3\}$.

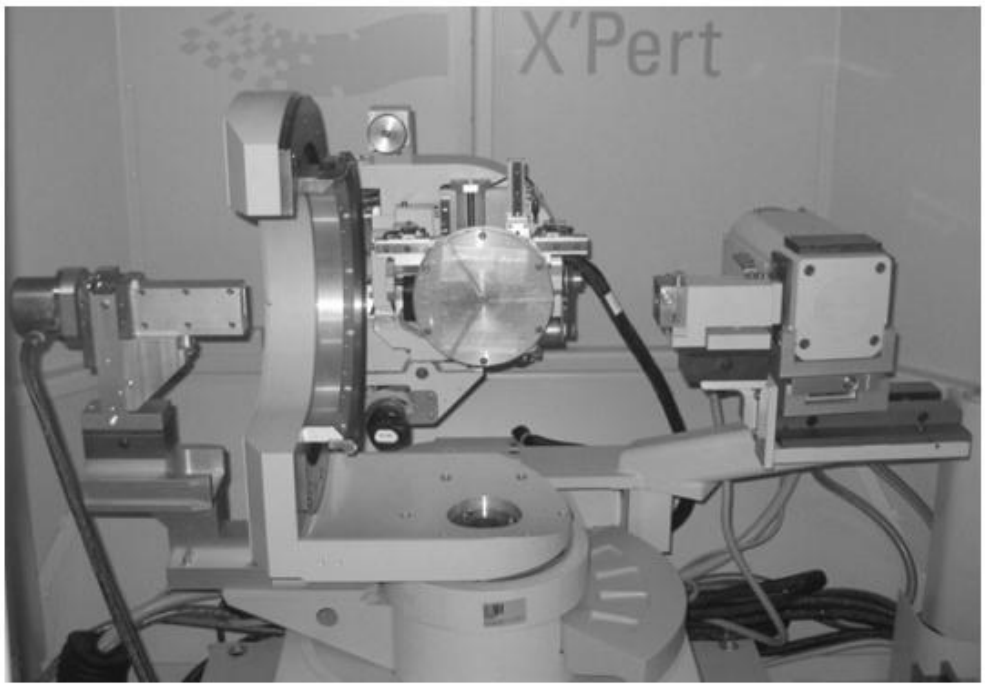

Figure 3.5 - *Texture measurement using Philips X' pert diffractometer equipped with texture goniometer*

For texture analysis, the samples were polished until the mid-section along the thickness using 180, 400, 1000 grit SiC papers. Cu Kα radiation was used for X-ray diffraction. Dedicated software MTEX Matlab quantitative texture analysis toolbox (Hielscher, 2008) was used to process the X-ray diffraction data and to produce the complete pole figures. During these calculations no symmetry was imposed to the pole figures.

From the processed data, a discrete set of 2212 grains were weighted, extracted and used for the input of the Visco-plastic self-consistent model (VPSC) developed by Lebenshon and Tome (Lebensohn R. A., 1993) (Lebensohn R. A., 1994) in order to simulate the evolution of crystallographic texture during the plastic deformation and analyze its influence on the mechanical behavior of the samples. During these calculations, the extension rate tensor and the critical resolved shear stress of the slip systems were kept constant (strain imposed and no hardening conditions). The experimental $\overline{R}$-values measured during the tensile test were used to define the extension rate tensor values.

4 Results and Discusion

4.1 Initial Material

In figure 4.1, the uniaxial true stress (σ)-true strain (ε) curves of as-received material loaded at θ =0°, 45°, and 90° from RD are presented. The initial sheet shows an anisotropic behavior characterized by higher flow stress when the sample is loaded at 0° than in the other two tested directions. The anisotropy has also expression on the higher uniform strain and R-value presented by the sample when is loaded at 0° from RD (Table 4.1). The high R values measured for all the tests (expressed by $\overline{R}$ = 1.59) are consistent with the values reported by Choi (Choi S. D., 2009) and shows that the strain along the width (ε_{22}) of the sample is significantly higher than along its thickness (ε_{33}). This corresponds to higher capability of the sheet to deform before failing due to excessive thickness reduction. The values of yield stress (σ_o) and the maximum tensile stress (σ_{max}) are consistent with the findings of several previous studies (Czerwinski, 2008) (Sekas, 2008) (Yang, 2008).

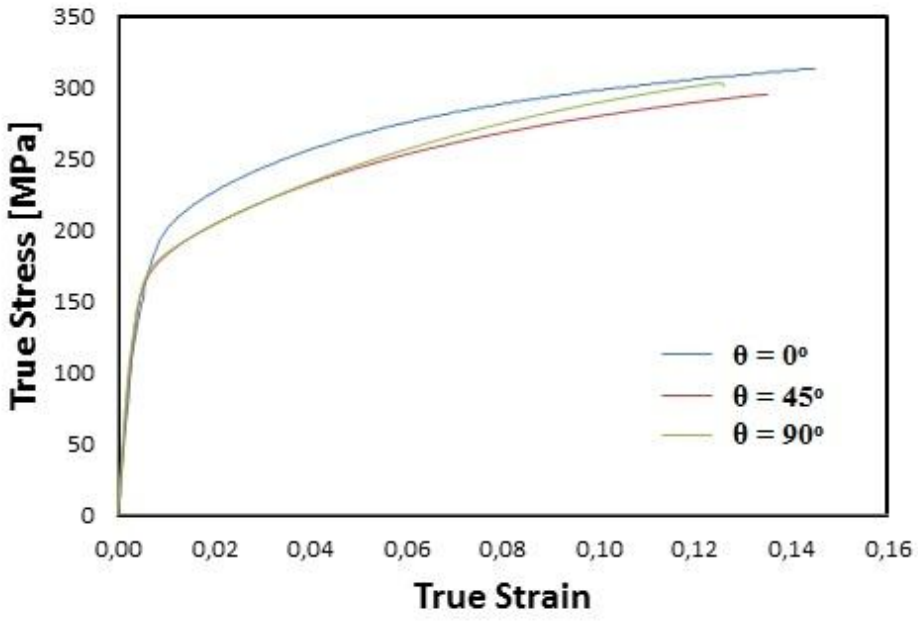

Figure 4.1 *- Tensile true stress - true Strain curves of the as-received AZ31 alloy tested at 0°, 45° and 90° from RD*

Table 4.1 *- Yield stress (σ_o), maximum stress (σ_{max}), uniform strain (ε_u), R-value, $\bar{R}$, and ΔR of the initial material tested in three different directions*

Test	Yield stress (σ_o) [MPa]	Max. Stress (σ_{max}) [MPa]	Uniform strain (ε_u)	R-value	Normal Anisotropy $\bar{R}$	Planar Anisotropy ΔR
0^o	228	312	0.143	1.79	1.59	0.07
45^o	205	295	0.135	1.56		
90^o	205	302	0.130	1.47		

In figure 4.2 are presented the microstructural observations performed by optical microscopy of the material before and after tensile test up to the maximum uniform strain value 0.14. The microstructure of the material is characterized by the presence of grains almost equiaxial and with an average size of around 8μm. In all the analyzed samples the grains were almost free of twins. Indeed, it is possible that the procedure used for sample preparation for optical microscopy produced some twins. However, the number of grains with these defects is very low and can be considered that the deformation of the AZ31 sheet occurs essentially by slip.

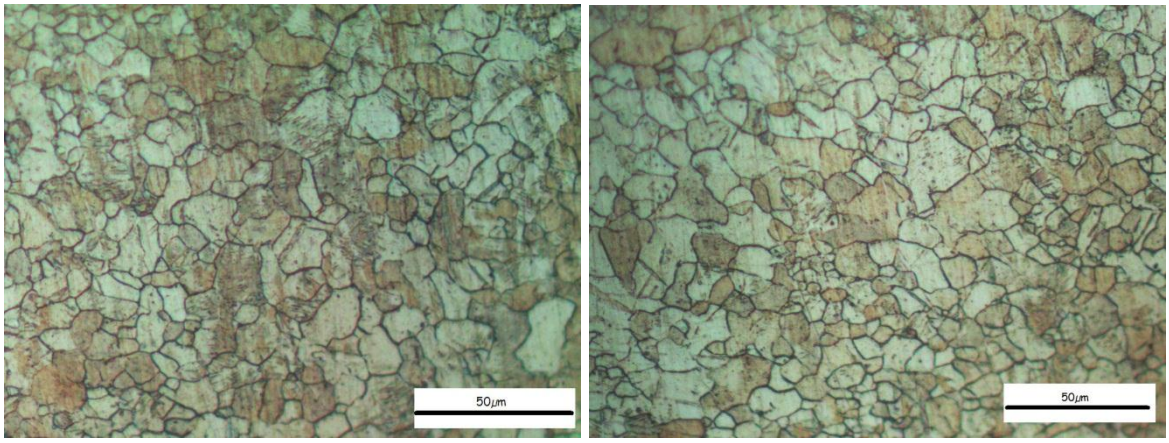

(a) (b)

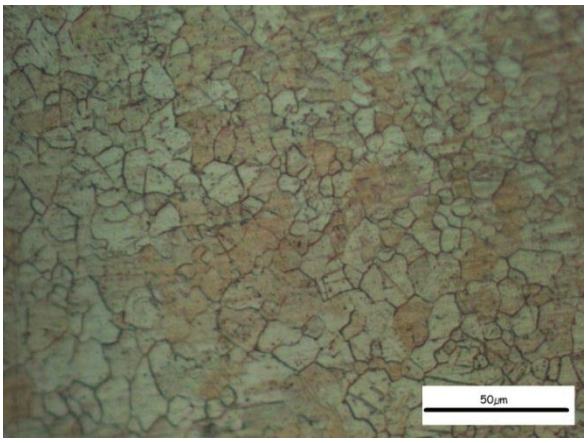

(c)

Figure 4.2 *- Microstructural observations by optical microscopy of the material after tensile test up to a strain value* $\varepsilon \approx 0.14$ *at (a)* 0^o*, (b)* 45^o*, (c)* 90^o*.*

The microstructural characterization of the material was complemented with TEM observations performed in the RD-TD (sheet plane), RD-ND (longitudinal plane), and TD-ND (transverse plane) planes of the sheet, before and after tensile tests. The results are presented in figures 4.3 and 4.4 and show that the initial material presents a very low dislocation density, which confirms that the material was supplied in the recrystallized state. In contrast, the deformed samples present a high dislocation density, homogeneously distributed through the grains without defining dislocation cells. This dislocation structure, that is similar in all samples and analyzed planes, is characteristic of the Mg alloys (Bryla, 2009) and reflects the low mobility of the dislocations in the structure of AZ31 due to their

low stacking fault energy (25mJ/m^2) (Lawrence, 1975) and the presence of solutes. During this analysis twins inside the grains were not observed. It is worth mentioning that the high elastic strain field associated with each dislocation made TEM analysis difficult, especially when these strain fields overlapped due to the high density of dislocations.

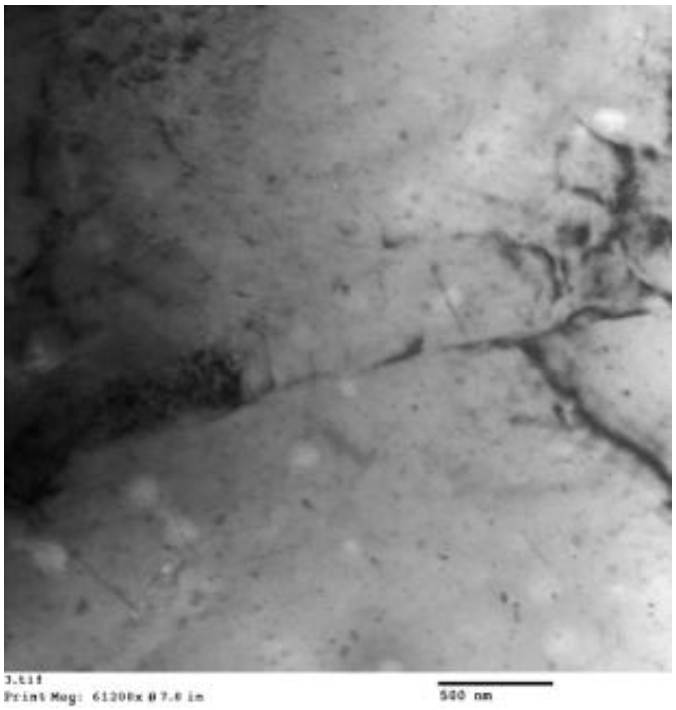

***Figure 4.3** - TEM image of the as-received material*

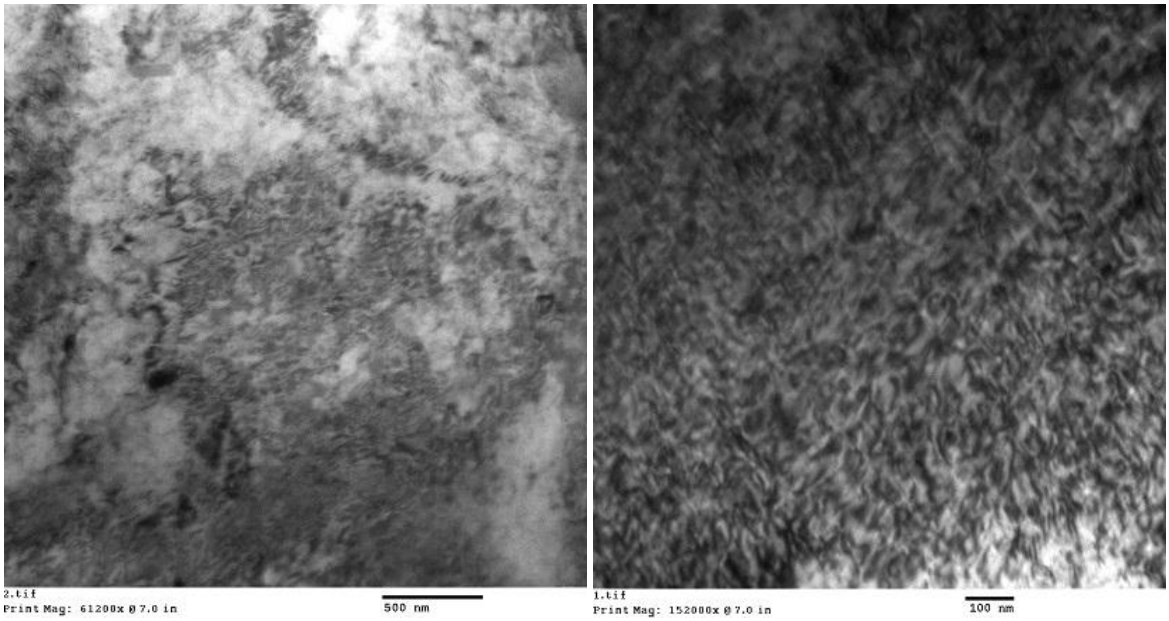

Figure 4.4 - *TEM image of the typical dislocation microstructure developed in the AZ31 after tensile test up to maximum uniform strain (sample loaded at 90^o).*

Figures 4.5 to 4.8 and in A.1 to A.4 present the crystallographic texture of the initial material and after the tensile test. The {0001},$\{10\bar{1}0\}$ pole figures and φ_2 = 0^o, 30^o, 60^o sections of Euler space shows that the as-received material has a strong {0001} <uvtw> fiber crystallographic texture component, typical of hot-rolled and annealed Mg sheets (Park, 2010) (Wang Y. H., 2003). During the tensile test the Mg grains rotates around the crystallographic c-axis giving rise to a strong $\{0001\}<10\bar{1}0>$ texture component, regardless the direction of the tensile tests. However, it is possible to verify that the $\{0001\}<10\bar{1}0>$ texture component is stronger for the samples loaded at 0^o than for 45^o and 90^o. In order to evaluate the influence of these differences on the mechanical behavior of the material, the evolution of the average Taylor factor (<M>) and the activity of the slip systems during the uniaxial tensile strain were computed using the VPSC code. In these calculations, it was assumed that the plastic deformation occurs by slip on the basal <a>, prismatic <a> and pyramidal <c+a> slip systems with normalized critical resolved shear stresses (CRSS) reported by (Proust, 2009) and presented in the table 4.2. It was also considered that twinning did not contribute to the plastic deformation of the material. This approximation is justified by the twinning-free microstructures observed by optical microscopy and TEM performed on the material and the absence of intensity reinforcement

of {0001} pole figures in the direction almost perpendicular (~86.6^{o}) to the ND direction of the sheet, typical when the tensile twinning is activated.

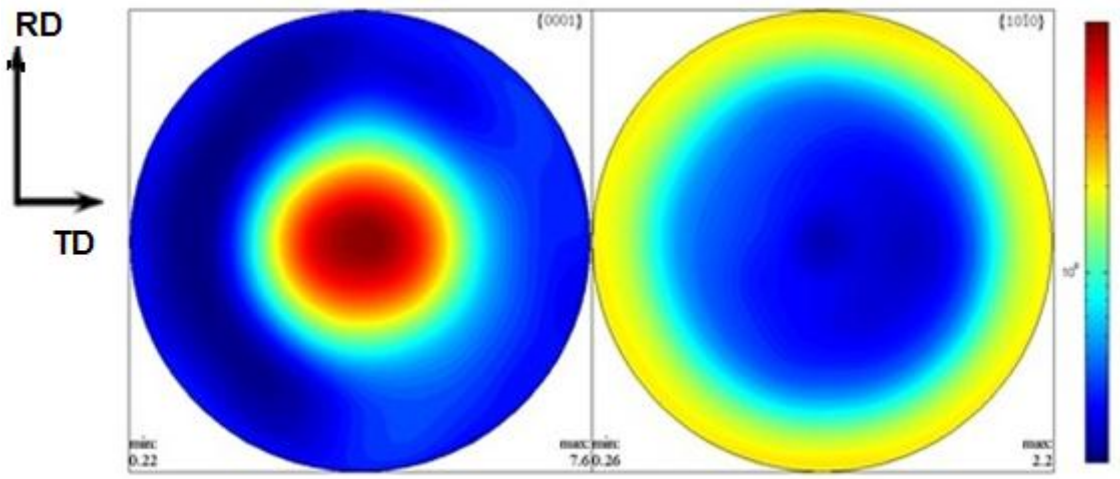

Figure 4.5 *- Experimental (a) {0001},{10$\bar{1}$0} pole figures for the as-received material. RD - rolling direction, TD - transverse direction.*

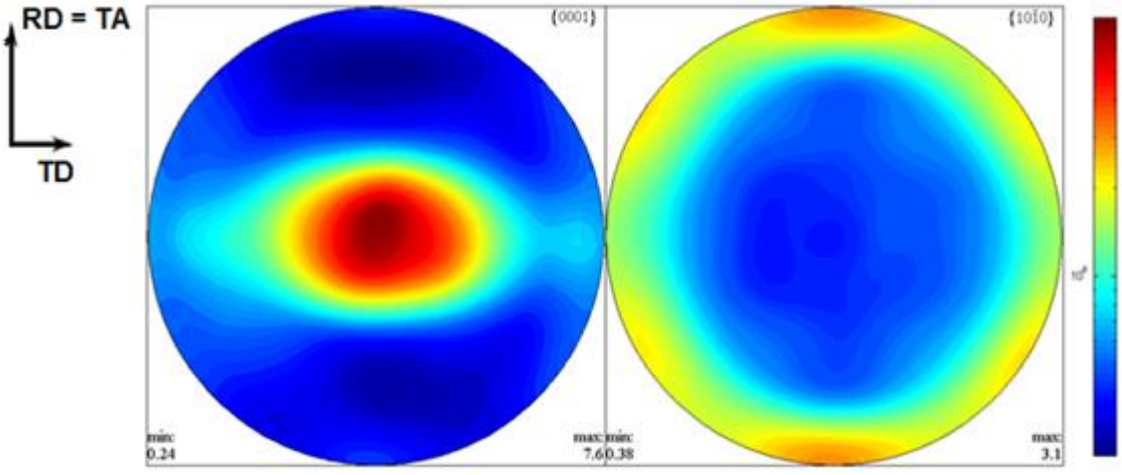

Figure 4.6 *- Experimental (a) {0001},{10$\bar{1}$0} pole figures for the material after tensile test up to the maximum uniform strain at 0^{o}. RD - rolling direction, TA - tensile axis, TD – transverse direction.*

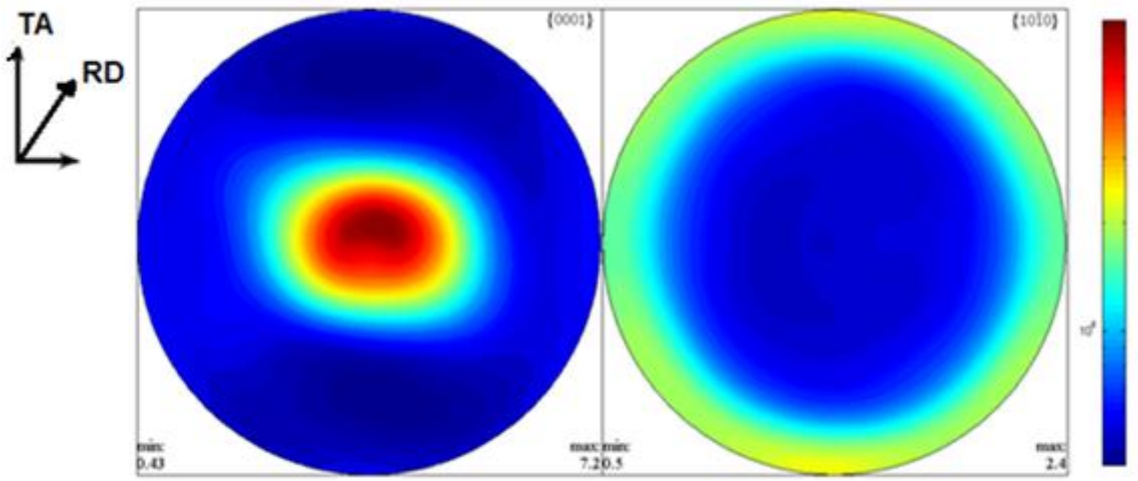

Figure 4.7 *- Experimental (a) {0001},{10$\bar{1}$0} pole figures for the material after tensile test up to the maximum uniform strain at 45^o. RD - rolling direction, TA - tensile axis.*

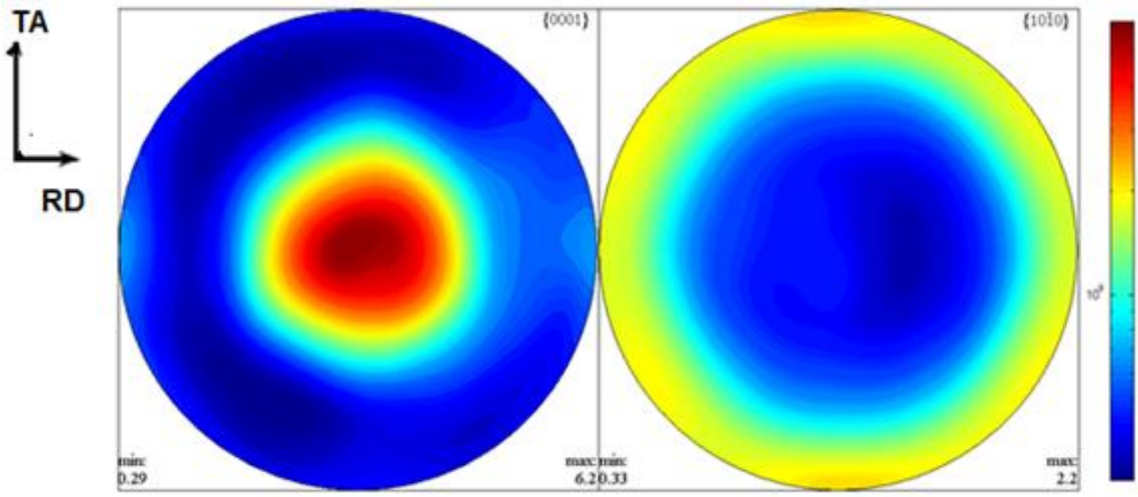

Figure 4.8 *- Experimental (a) {0001},{10$\bar{1}$0} pole figures for the material after tensile test up to the maximum uniform strain at 90^o. RD - rolling direction, TA - tensile axis.*

Table 4.2 - *Normalized critical resolved shear stress (CRSS) of the slip systems used in the VPSC calculations (Proust, 2009)*

Slip system	Normalized CRSS
Basal <a> ({0001}<10$\bar{1}$0>)	1.0
Prismatic <a> ({10$\bar{1}$0}<11$\bar{2}$0>)	2.9
Pyramidal <c+a> ({11$\bar{2}$2} <11$\bar{2}$3>)	5.2

The results of polycrystal plasticity code are presented in figures 4.9 to 4.12 and table 4.3. The textures predicted by the model for the analyzed samples (figures 4.9 to 4.11 and A.5 to A.7 in appendix) present good qualitative agreement with the experimental textures showing that VPSC model can be used to analyze the influence of the crystallographic texture on the mechanical behavior of Mg sheet. Indeed, from a quantitative point of view, the predicted textures are, as usual (Kocks, 1998), sharper than the experimental ones due to the discrete nature of the model but all the simulated pole figures present the strong {0001}<10$\bar{1}$0> component that, for $\theta = 0^o$, is a little more intense than for $\theta = 45^o$ and 90^o. These differences give rise to a higher Taylor factor for 0^o than for the other two directions (fig. 4.12). In fact, all the samples present a continuous increase of <M> value with the strain that correspond to a stronger contribution of the crystallographic texture evolution for the strain hardening during the tensile test (textural hardening) but for each strain value the orientation assumed by the grains in the sample deformed at 0^o opposes more efficiently to the plastic deformation. Quantitatively these results reflect the hierarchy of the experimental σ-ε curves of figure 4.1 strongly suggesting that the crystallographic texture has an important role on the anisotropic flow stress observed during the tensile tests performed to the initial material.

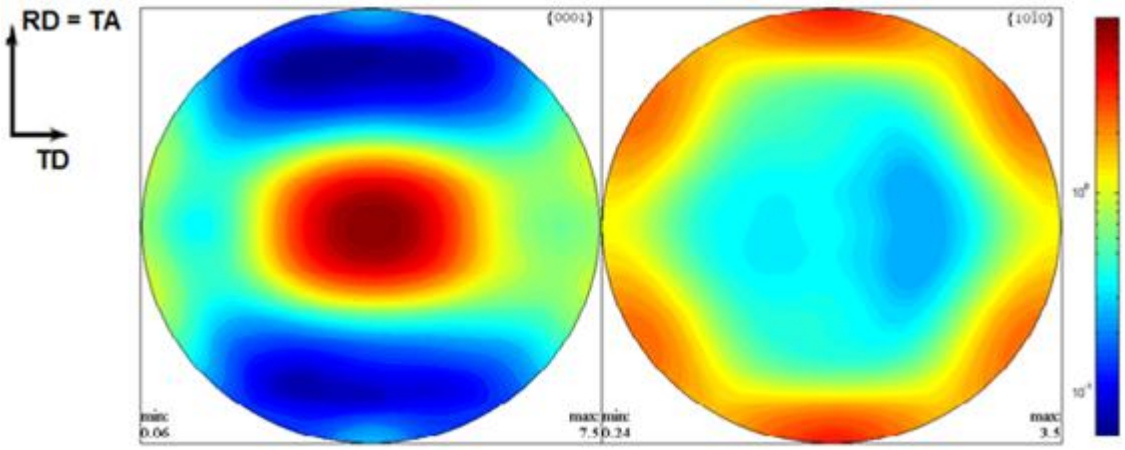

Figure 4.9 *- Simulated (using VPSC code) (a) {0001},{10$\bar{1}$0} pole figures for the material after tensile test up to the maximum uniform strain at 0^o. RD - rolling direction, TA - tensile axis, TD – transverse direction.*

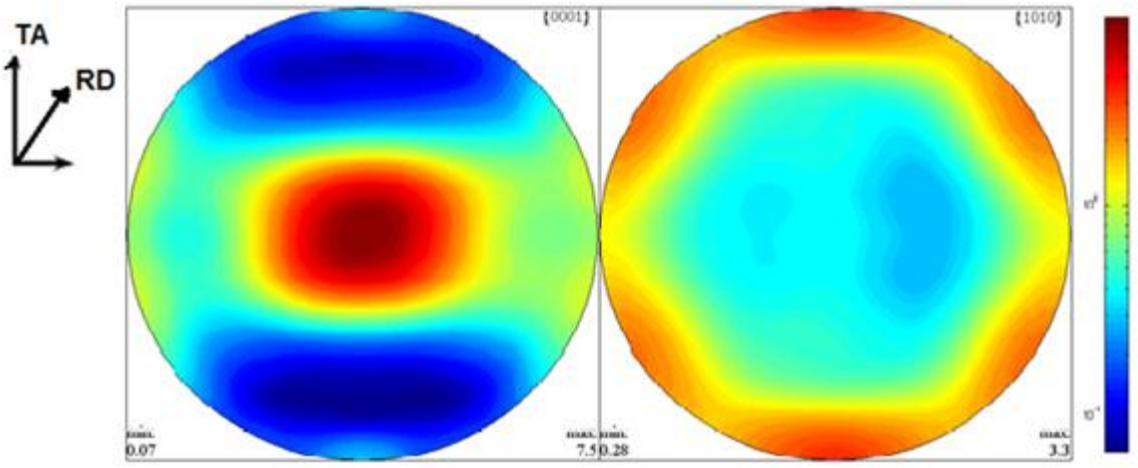

Figure 4.10 *- Simulated (using VPSC code) (a) {0001},{10$\bar{1}$0} pole figures for the material after tensile test up to the maximum uniform strain at45^o. RD - rolling direction, TA - tensile axis.*

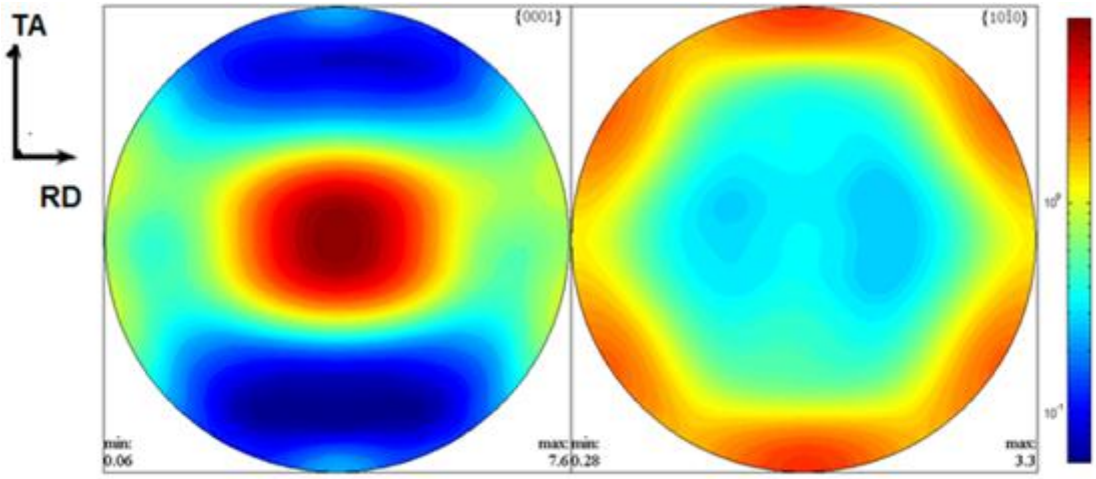

Figure 4.11 *- Simulated (using VPSC code) (a) {0001},{10$\bar{1}$0} pole figures for the material after tensile test up to the maximum uniform strain at 90^{o}. RD - rolling direction, TA - tensile axis.*

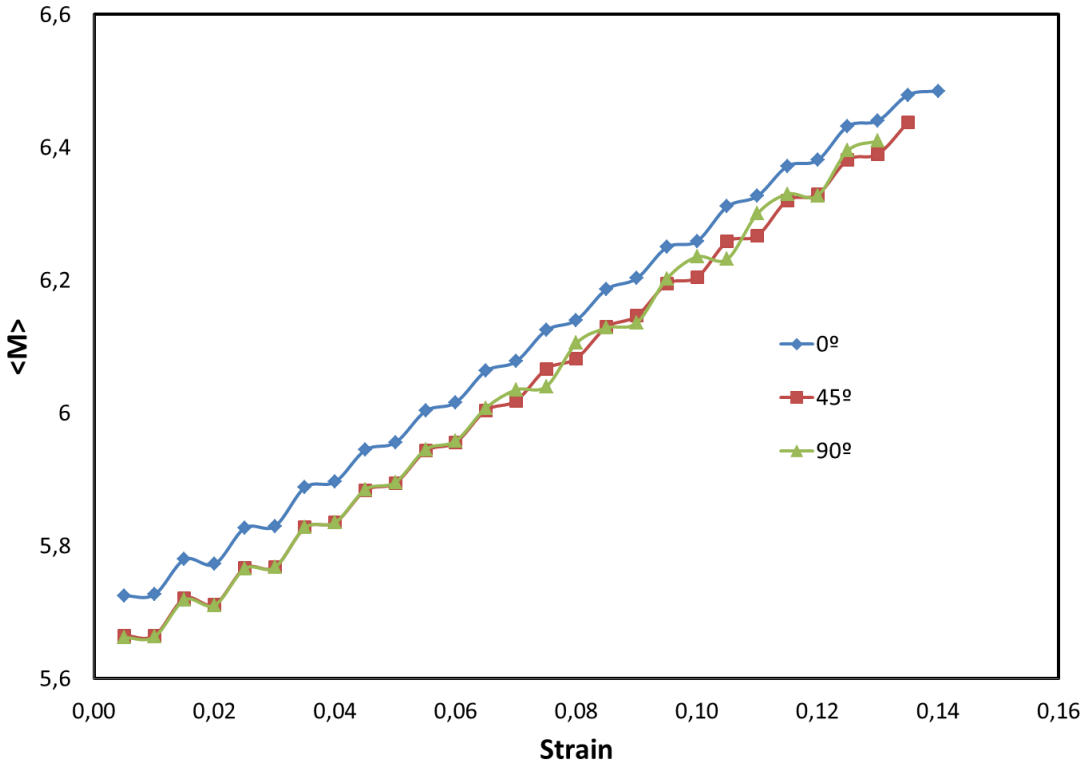

Figure 4.12 *- Taylor factor - strain curves predicted by the VPSC model for initial material deformed in tensile test in three different test directions.*

In table 4.3 is presented the activity of the slip systems computed by VPSC code for the three analyzed directions at different tensile strain values. It is possible to verify that the

accommodation of the plastic deformation occurs essentially through the activation of the basal and prismatic slip systems as reported by several authors (Choi S. D., 2009) (Proust, 2009) (Wang Y. H., 2003). More specifically, for all the directions and strain values, the basal <a> is the most activated slip systems but its contribution to the plastic deformation of the grains decreases with the strain and is lower for 0^o than for the other two tensile directions. This evolution can justify the <M> - ε curves computed by the polycrystal model. Indeed, by comparing figure 4.12 and the values in the table 4.3 one may verify that the increase of the Taylor factor is associated with a decrease of activity in the basal slip planes and an increase of activity in the prismatic slip plane. This shows that the orientation of the basal and the prismatic planes with respect to the tensile direction has a strong influence on the flow stress during the tensile test. Taking into account that the basal plane contains the slip systems with lower critically resolved shear stress, is expected that the changes of activity in this plane have higher impact on the flow stress than the changes of activity in other slip planes. In this case, the increase of the fraction of Mg grains with c-axis parallel to ND of the sheet corresponds to a decrease of resolved shear stress in the basal planes and, therefore, should be decisive for the increase of tensile flow stress. This hypothesis is consistent with the distortion (contraction) of maximum of intensity on the center of {0001} pole figures experimentally observed for samples loaded at 0^o and 45^o and in all simulated pole figures. However, this effect is not clear for 90^o experimental pole figures and should be confirmed in the future work.

Table 4.3 - *Activity of the slip systems computed by VPSC code for the three analyzed directions*

Strain	Activity								
	0º			45º			90º		
	Basal	Prismatic	Pyramidal	Basal	Prismatic	Pyramidal	Basal	Prismatic	Pyramidal
0.005	0.80	0.20	0.00002	0.83	0.18	0.00001	0.82	0.17	0.00001
0.025	0.78	0.22	0.00002	0.80	0.19	0.00002	0.81	0.19	0.00002
0.045	0.77	0.23	0.00002	0.80	0.21	0.00002	0.79	0.21	0.00002
0.065	0.75	0.25	0.00003	0.77	0.23	0.00003	0.77	0.23	0.00003
0.085	0.72	0.28	0.00005	0.75	0.25	0.00004	0.74	0.25	0.00004
0.105	0.70	0.30	0.00007	0.72	0.28	0.00006	0.72	0.28	0.00006
0.125	0.67	0.33	0.00011	0.69	0.31	0.00010	0.69	0.31	0.00009
0.13	0.66	0.34	0.00011	0.68	0.32	0.00010	0.68	0.31	0.00009
0.135	0.65	0.35	0.00013	0.67	0.33	0.00012	---	---	---
0.14	0.64	0.35	0.00014	---	---	---	---	---	---

4.2 Material after pre-deformation

The true stress (σ) - true strain (ε) curves of AZ31 alloy sheet obtained by tensile test performed at different angles (θ) from RD after pre-deformation up to 0.07 tensile strain in the rolling direction are presented in figure 4.13. For comparison, it is also presented the σ – ε curve of material during the pre-deformation at 0^o from RD. The predominant feature of these curves is the decrease of the flow stress with increase of the reloading angle. Indeed, when the reloading direction is parallel to the prestrain direction ($\theta = 0^o$), which corresponds to a monotonic interrupted test, the flow stress in both tests are similar and the respective σ – ε curves superimpose. However, when the angle between the pre-deformation and the reloading increases, the flow stress in the second strain path decreases, especially in the beginning of the test.

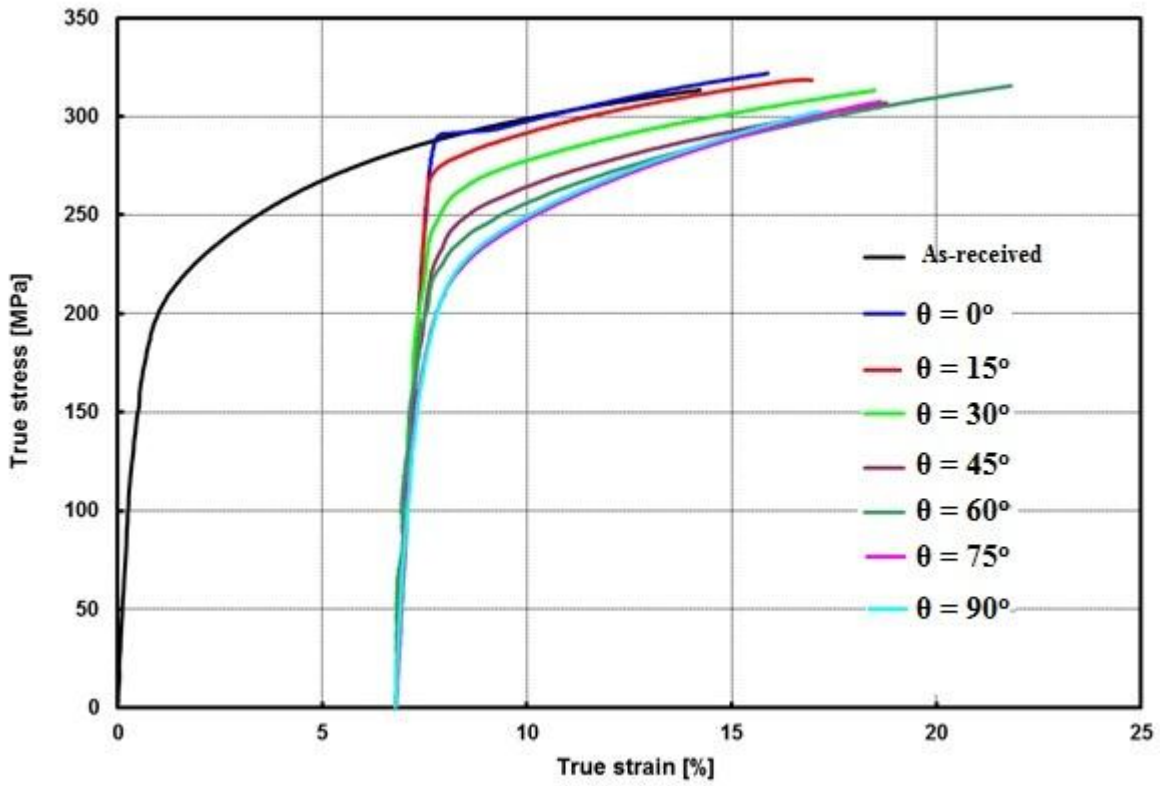

Figure 4.13 *– Tensile true stress (σ) - true strain (ε) curves at 0°, 15°, 30°, 45°, 60°, 75° and 90° of AZ31 after pre-deformation up to 0.07. The curve for as-received material is also presented.*

Another trend in figure 4.13 is the increase of the total uniform strain of the reloaded sample when compared with the prestrained one (table 4.4). These differences can be justified by the higher R-values (and $\overline{R}$) measured for the pre-deformed samples that reflect lower sample thickness reduction during the tensile tests.

Table 4.4 *- Yield stress (σ_o), maximum stress (σ_{max}), uniform strain (ε_u), R-value, $\overline{R}$ and ΔR of the pre-deformed material reloaded in different directions*

Test	Yield stress (σ_o) [MPa]	Max. Stress (σ_{max}) [MPa]	Uniform strain (ε_u)	R-value	Normal anisotropy $\overline{R}$	Planar anisotropy ΔR
0°	290	332	0.159	1.81	2.20	-0.78
15°	282	320	0.170	2.45		
30°	270	320	0.185	1.93		
45°	250	312	0.189	2.57		
60°	241	311	0.219	1.94		
75°	232	305	0.188	1.86		
90°	231	308	0.171	1.78		

As mentioned before in chapter 2, the change of strain path promotes changes in the activity of the available slip systems that, depending of the amplitude of the applied changes (which can be characterized by α-parameter value), can strongly influence the mechanical response of the material. For α = 1, that corresponds to monotonic test, i.e. when the sample is unloaded and reloaded in the same tensile direction, the same slip systems are activated before and after reloading. For α = -1, the strain is reversed (corresponding to a Bauschinger type test), and the slip systems are reactivated in opposite directions during the two loadings. The intermediate situation (α = 0) corresponds to an amplitude of strain path change which activates different slip systems during the prestrain and reloading. For an isotropic material (with R = 1) and the tensile-tensile test sequence, α covers the range of values from 1 to -0.5 (curve (a) of fig. 4.14). More specifically, α = 1, 0 and -0.5 corresponds to the test performed at θ = 0°, 55° and 90°. For materials with R ≠ 1, as the AZ31 investigated sheet, these α-values occur for different loading angle. Namely, for R = 2.2 (table 4.4), the reloading at 0°, 47° and 90° correspond to a α-value equal to 1, 0, and -0.83, respectively (curve (b) of fig. 4.14).

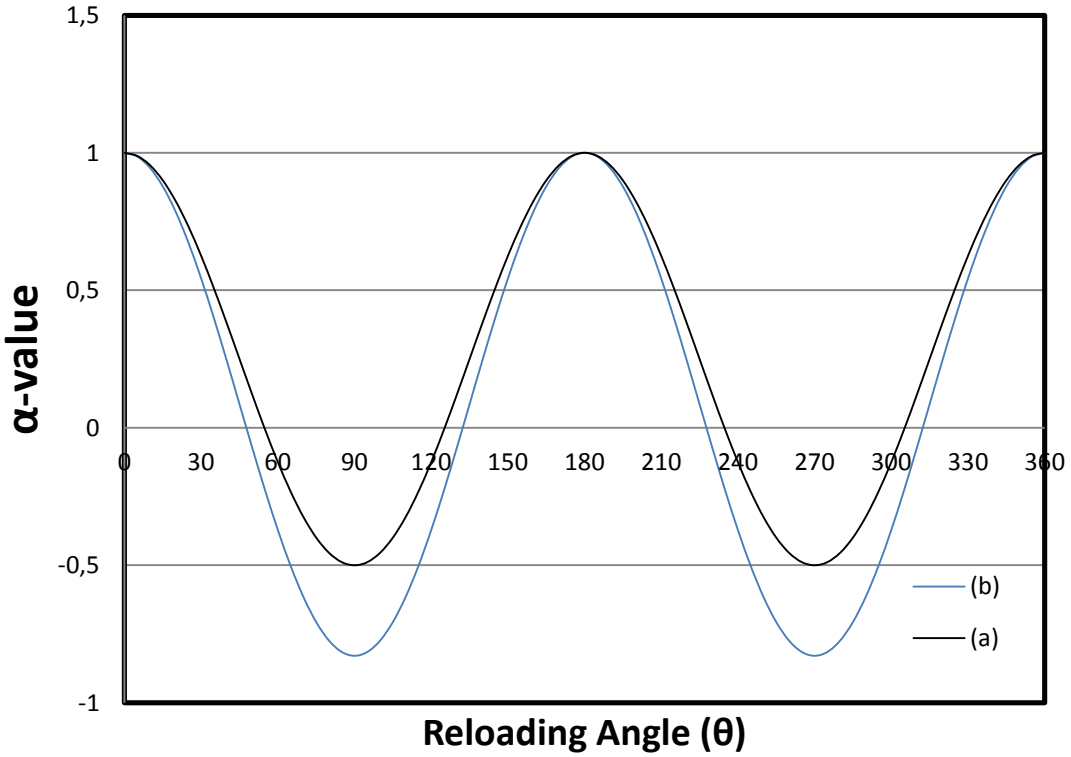

Figure 4.14 *- Evolution of α parameter with the reloading angle for (a) isotropic (R =1) and (b) anisotropic (R = 2.2) material deformed in tensile-tensile test.*

The results of the previous figure show that the reloading at 0^o to 47^o requires the progressive activation of new slip systems that were latent during the prestrain and should be responsible for an increase of reloading yield stress. By contrast, for the reloading angles between 47^o and 90^o an increased number of slip systems are reactivated in the reverse direction during the reloading that should promote a progressive decrease of the reloading yield stress. For dislocation cell-forming materials (as Al, Cu, low carbon steels etc.) these changes in activity of the slip systems occurs with the replacement of the dislocation structures developed during the prestrain by a typical dislocation structure of the new strain path. For no cell-forming materials, as the one investigated in this work, the effect of these changes in the activity of the slip systems during the strain path change give rise to similar dislocation structure after the reloading at different angles. Indeed, all the reloaded samples present similar dislocation microstructure (fig. 4.15), characterized by homogeneous distribution of dislocations and no specific feature that can justify the differences in mechanical behavior during the reloading was observed.

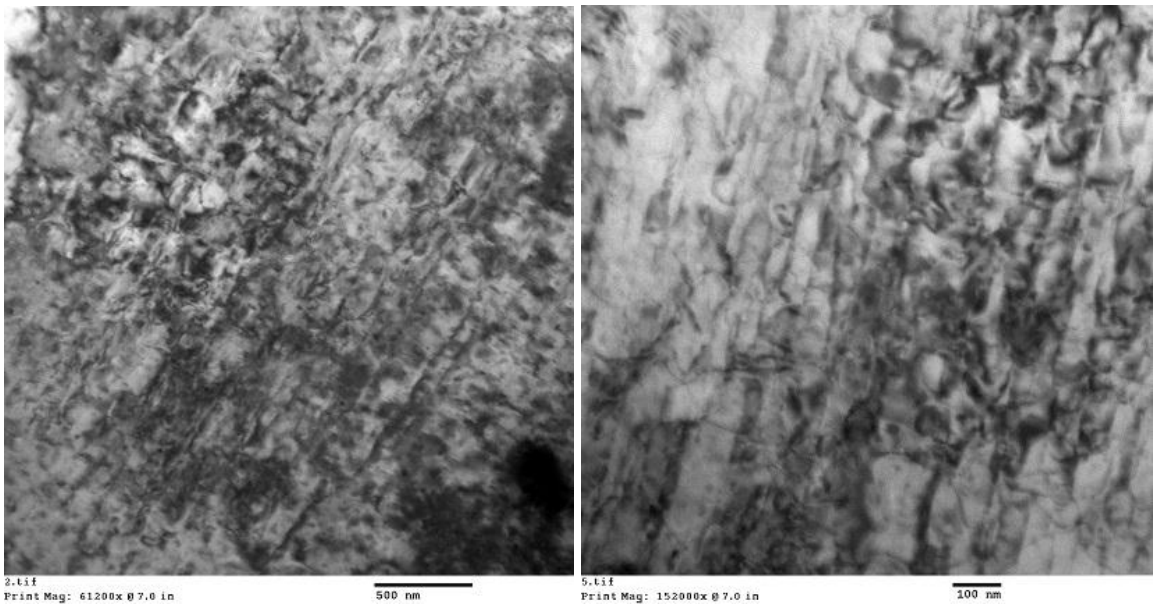

Figure 4.15 *- TEM image of the typical dislocation microstructure developed in the AZ31 after reloading up to maximum uniform strain (left: sample reloaded at 45^o and right: sample reloaded at 90^o).*

By contrast, the crystallographic textures presented by the material reloaded at 0^o, 45^o and 90^o are different (fig. 4.16 to 4.18 and A.8 to A.10). For $\theta = 0^o$, the final texture presents the strong {0001}<$10\bar{1}0$> component, similar to the one observed in as-received material after tensile test. For $\theta = 45^o$, the pole figures show the superposition of the {0001}<$10\bar{1}0$> component developed during reloading (that appears as a reinforcement along the tensile direction) with the one developed during prestrain (that appears as a reinforcement along 45^o from tensile direction). For $\theta = 90^o$, the reactivation of slip systems during the second path is in the opposite direction and gives rise to reverse grain rotations and to a final texture that is similar to the one observed in as-received material ({0001}<uvtw> fiber texture).

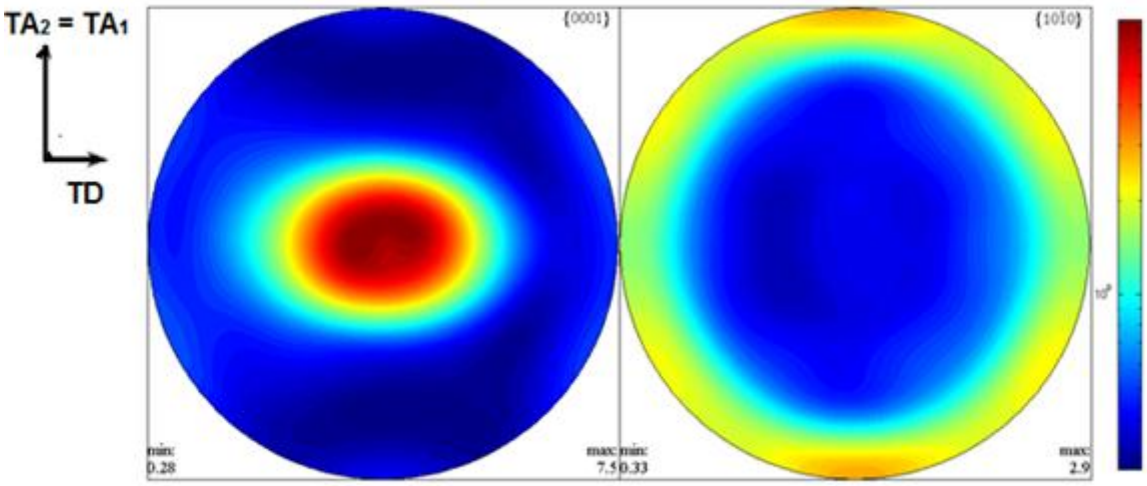

Figure 4.16 *- Experimental (a) {0001},{10$\bar{1}$0} pole figures for the material after reloading at 0^o. RD - rolling direction, TA_1 - tensile axis for the 1st path, TA – Tensile axis for the 2nd path TD – transverse direction.*

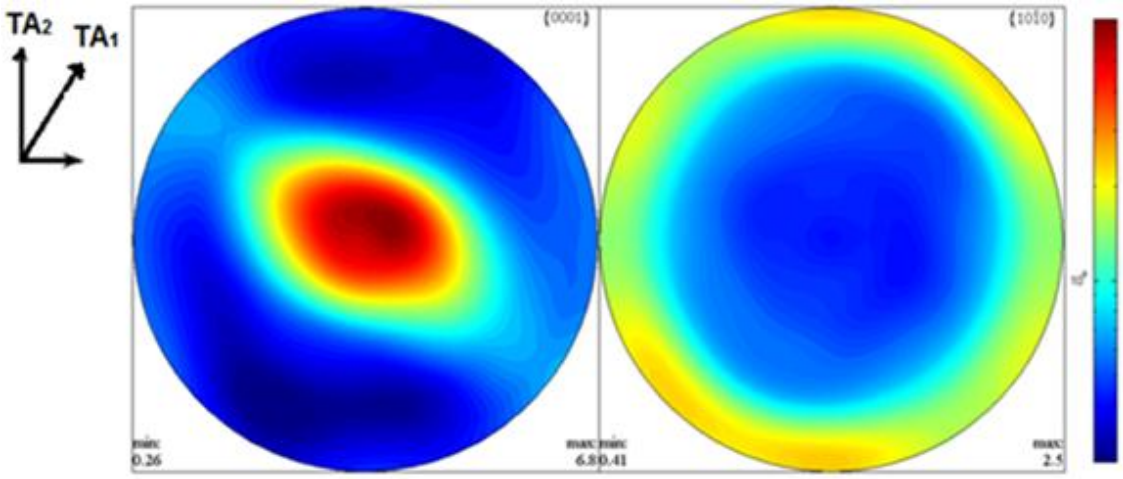

Figure 4.17 - *Experimental (a) {0001},{10$\bar{1}$0} pole figures for the material after reloading at 45^o. TA_1 - tensile axis for the 1st path, TA_2 – Tensile axis for the 2nd path TD.*

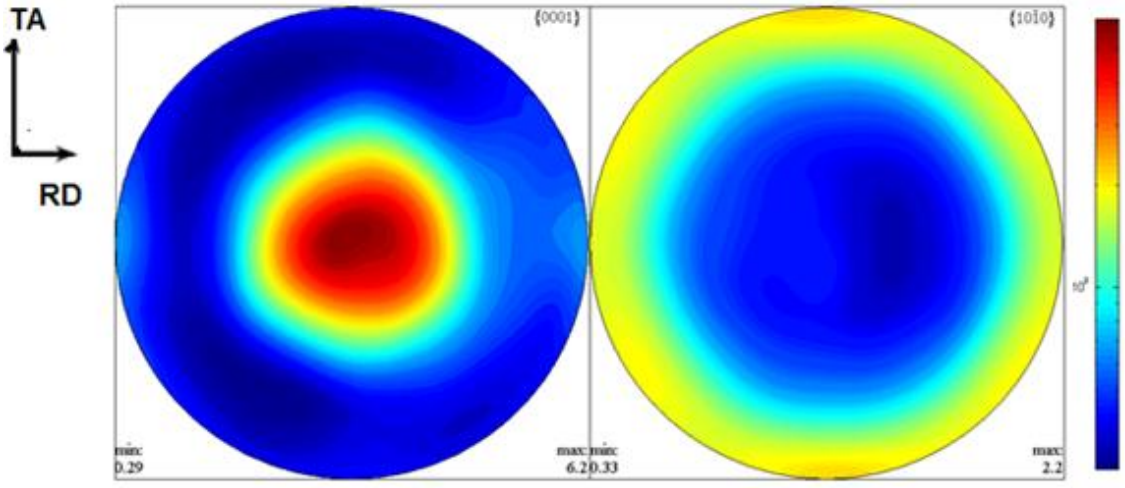

Figure 4.18 *- Experimental (a) {0001},{10$\bar{1}$0} pole for the material after reloading at 90^o. RD - rolling direction, TA - tensile axis, TD – transverse direction.*

The contribution of these differences in crystallographic texture on the mechanical behavior during the reloading were analyzed (as in previous section) through simulations using VPSC model. The simulated textures are presented in figures 4.19 to 4.21 and A.11 to A.13, in appendix. For all the samples good qualitative agreement was obtained between

the simulated and experimental textures, showing that VPSC captures the main changes of texture during the reloading and, as for the as-received material, can be used to analyze the mechanical behavior of Mg sheet during the reloading.

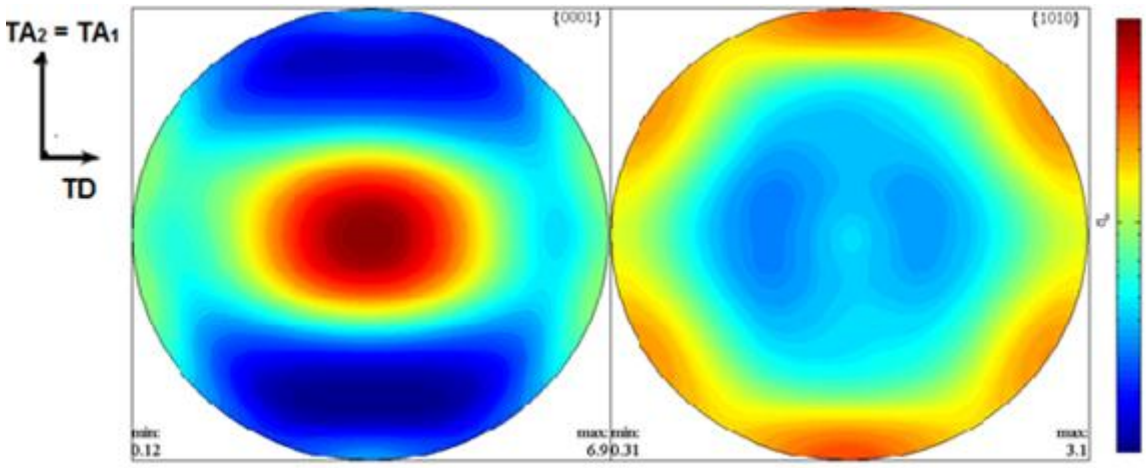

Figure 4.19 – *Simulated (using VPSC) (a) {0001},{$\mathbf{10\bar{1}0}$} pole figures for the material after reloading at 0°. TA_1 - tensile axis for the 1st path, TA – Tensile axis for the 2nd path TD – transverse direction.*

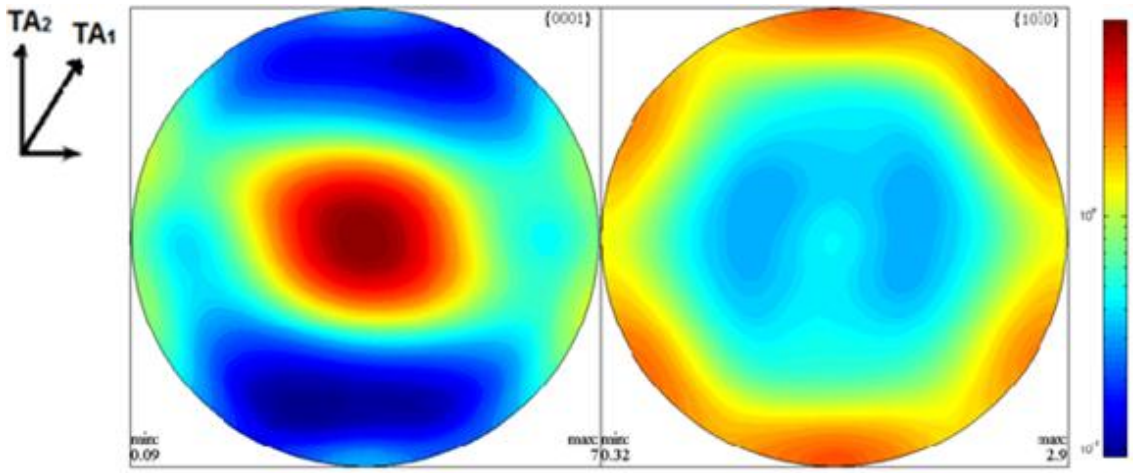

Figure 4.20 - *Simulated (a) {0001},{$\mathbf{10\bar{1}0}$} pole figures for the material after reloading at 45°. TA_1 - tensile axis for the 1st path, TA_2 – Tensile axis for the 2nd path TD.*

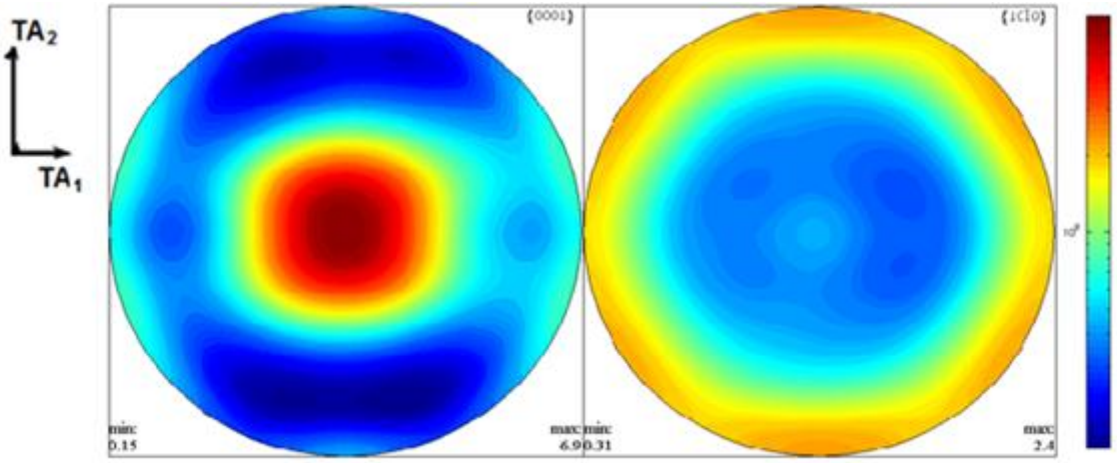

Figure 4.21 *- Simulated (a) {0001},{**10$\bar{1}$0**} pole for the material after reloading at 90^o. RD - rolling direction, TA - tensile axis, TD – transverse direction.*

Also, the comparison of the <M> - ε curves (fig. 4.22) with the evolution of the flow stress during the reloading (fig. 4.13) shows a good qualitative agreement. Namely, higher values of Taylor factor corresponds to a higher flow stress in the beginning of the second path, for all the analyzed directions. This is a strong indication that the crystallographic texture has a major influence on the differences in the mechanical behavior observed during the reloading of Mg alloy sheet.

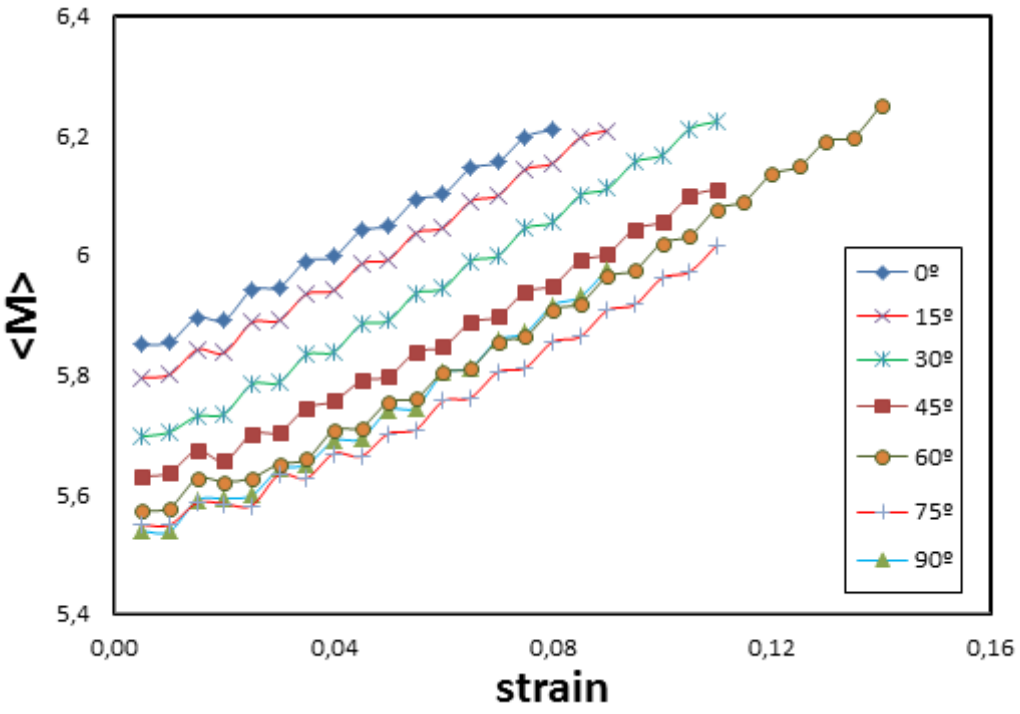

Figure 4.22 *- The <M> - ε curves after reloading at different test directions predicted by the VPSC model in the strain imposed condition*

Another analysis that can be performed is about the influence of the activity of slip systems on the evolution of the Taylor factor during the second strain path. The results of VPSC model in table 4.6 to 4.8 shows that, as observed for as-received material, the plastic deformation during reloading of Mg sheet occurs mainly by activation of basal <a> and prismatic <a> slip systems and the increase of the <M> value occurs when the activity of the basal <a> system decreases. This is in agreement with the proposed hypothesis that the orientations of the c-axis of the grains relatively to the normal direction of the sheet has a strong influence on the activity of the basal slip systems and, therefore, on the flow stress during tensile test of Mg sheet.

Table 4.5 - *Activity of the slip systems computed by VPSC code for samples reloaded at 0º, 15º and 30º.*

Strain	Activity								
	0º			15º			30º		
	Basal	Prismatic	Pyramidal	Basal	Prismatic	Pyramidal	Basal	Prismatic	Pyramidal
0.005	0.77	0.22	0.00003	0.78	0.22	0.00002	0.80	0.20	0.00001
0.020	0.76	0.24	0.00003	0.77	0.23	0.00003	0.79	0.21	0.00002
0.035	0.74	0.26	0.00004	0.75	0.25	0.00003	0.77	0.22	0.00002
0.050	0.72	0.28	0.00004	0.73	0.26	0.00004	0.75	0.24	0.00003
0.065	0.70	0.30	0.00005	0.72	0.28	0.00005	0.74	0.26	0.00003
0.080	0.69	0.31	0.00006	0.70	0.30	0.00006	0.72	0.28	0.00004
0.095	---	---	---	---	---	---	0.70	0.30	0.00005
0.11	---	---	---	---	---	---	0.68	0.32	0.00006

Table 4.6 - Activity of the slip systems computed by VPSC code for samples reloaded at 45º and 60º.

Strain	Activity					
	45º			60º		
	Basal	Prismatic	Pyramidal	Basal	Prismatic	Pyramidal
0.005	0.80	0.19	0.00001	0.81	0.19	0.00001
0.020	0.80	0.21	0.00002	0.80	0.19	0.00001
0.035	0.78	0.22	0.00002	0.79	0.20	0.00001
0.050	0.77	0.23	0.00002	0.78	0.22	0.00002
0.065	0.75	0.25	0.00003	0.77	0.23	0.00002
0.080	0.74	0.26	0.00003	0.75	0.25	0.00003
0.095	0.72	0.28	0.00004	0.74	0.26	0.00003
0.11	0.70	0.29	0.00005	0.72	0.28	0.00004

Table 4.7 - Activity of the slip systems computed by VPSC code for samples reloaded at 75º and 90º.

Strain	Activity					
	75º			90º		
	Basal	Prismatic	Pyramidal	Basal	Prismatic	Pyramidal
0.005	0.81	0.18	0.00001	0.82	0.17	0.00001
0.020	0.80	0.19	0.00001	0.82	0.18	0.00001
0.035	0.79	0.21	0.00001	0.81	0.29	0.00001
0.050	0.78	0.22	0.00002	0.80	0.20	0.00002
0.065	0.77	0.23	0.00002	0.79	0.21	0.00002
0.080	0.76	0.24	0.00003	0.77	0.23	0.00003
0.095	0.74	0.25	0.00003	---	---	---
0.11	0.73	0.27	0.00004	---	---	---

5 Conclusions

The influence of the strain path change on the mechanical behavior of AZ31 alloy was studied. For that, AZ31 sheets were pre-strained and afterwards eight different orientations (with respect to the RD) were selected to conduct the tensile test. The influence of the dislocation structure and crystallographic texture during the plastic deformation on the mechanical behavior of the material during both the uniaxial tensile tests was analyzed using transmission electron microscopy (TEM) and X-ray diffraction. The visco-plastic self-consistent (VPSC) model was used to quantify the effect of crystallographic texture on the stress-strain curves obtained by tensile tests performed.

Based on the results, the following conclusions can be drawn:

I. The as-received material showed anisotropic properties in different test directions characterized by anisotropy in flow stress, uniform strain and R-value. For all the investigated directions (0^o, 45^o, 90^o), the material loaded at 0^o showed higher values for each of them. The high R value measured for all the tests ($\overline{R}$ = 1.59) corresponds to a higher capability of the sheet to deform before failing due to excessive thickness reduction.

II. Optical microscopic observations of the material before and after tensile test depict that, the microstructure of the material comprised of almost equiaxial grains. The volume fraction of twins observed in the grains was insignificant suggesting that, the deformation process was essentially governed by slip.

III. TEM observations of the as-received material before and after the tensile test showed that, the initial material was characterized by a low dislocation density whereas the deformed material presented a high dislocation density without defining dislocation cells. This reflects the low mobility of the dislocation in the material essentially due to their low stacking fault energy and presence of solute. The analysis also confirmed the presence of twins in the grains was insignificant.

IV. Texture analysis on the as-received material before tensile test showed that, the as-received material has a strong {0001} <uvtw> fiber crystallographic texture

component. After tensile test, {0001}<10$\bar{1}$0> texture component was observed to be predominant for all analyzed test direction where it was stronger for material loaded at 0^o than the other two test directions. The results were qualitatively complemented using polycrystal model (VPSC code) suggesting that VPSC model can be used to compute the influence of the crystallographic texture on the mechanical behavior of Mg sheet. The stronger {0001}<10$\bar{1}$0> texture component for material loaded at 0^o contributed to its higher <M> value than the other two test directions. Quantitatively these results reflected the hierarchy of the experimental σ-ε curves strongly suggesting that the crystallographic texture has an important role on the anisotropic flow stress observed during the tensile tests performed to the initial material.

V. Calculation of activity of slip system (using VPSC) for as-received material before and after tensile test revealed that, plastic deformation occurs essentially through the activation of the basal and prismatic slip systems. However, the contribution to the plastic deformation of basal slip decreases with the strain and is lower for 0^o than for the other two tensile directions strongly justifying the <M> - ε curves computed by the polycrystal model. This shows that the orientation of the basal and the prismatic planes with respect to the tensile direction has a strong influence on the flow stress during the tensile test. The effect was observed for samples loaded at 0^o and 45^o and in all simulated pole figures. However, this effect was not clear for 90^o experimental pole figures.

VI. The material pre-deformed and reloaded at different angles from RD presented anisotropy in flow stress, uniform deformation and R-value. The predominant feature of true stress – true strain curves was the decrease of the flow stress with increase of the reloading angle. The material after reloading presented higher uniform strain than the prestrained one justified by their higher R-value ($\overline{R}$ = 2.20) that reflects a decrease of the sheet thickness reduction during loading.

VII. The changes in the activity of slip systems promoted by strain path change (where the amplitude of the change is characterized by α parameter) for the material (pre-deformed and reloaded at different angles) did not show any effect on the dislocation structure observed by TEM. The structure was characterized by a homogeneous distribution of dislocations (similar to the initial material) and no

specific feature that can justify the differences in mechanical behavior during the reloading was observed. However, as observed for as-received material, the plastic deformation during reloading of Mg sheet occurs mainly by activation of basal <a> and prismatic <a> slip systems and the increase of the <M> value occurs when the activity of the basal <a> system decreases.

VIII. The <M> - ε curves for material after reloading at different test directions predicted by the VPSC model showed that, higher values of Taylor factor corresponds to a higher flow stress in the beginning of the second path, for all the analyzed directions. That strongly suggests that the crystallographic texture has a major influence on the differences in the mechanical behavior observed during the reloading of Mg alloy sheet (as concluded for initial material).

6 Proposals for further study

Based on the results obtained, a proposal is given below which may improve the understanding of the behavior of these alloys:

- Similar studies should be conducted on AZ31 alloys with different prestrain value and varying temperatures. The increase of the prestrain value increases the population of dislocations, mutual interactions whereas the temperature has the opposite effect. Moreover, the increase of temperature promotes the activity of non-basal slip systems. So change of prestrain value at different temperature can be an interesting aspect to explore in order to improve the understanding of the deformation mechanism (essentially the contribution of dislocations relative to the crystallographic texture) of Mg alloys.

7 Bibliography

Agnew, S. C., C. N. Tome., D. W. Brown., T. M. Holden., S. C. Vogel (2003). Study of slip mechanisms in magnesium alloy by neutron diffraction and modelling. Scripta Materialia, 48, 1003-1008.

Ahzi, S., S. M'Guil. (2008). A new intermediate model for polycrystalline viscoplastic deformation and texture evolution. Acta Materialia, 56(19), 5359-5369.

Alan, A. L. (2003). Recent magnesium alloy development for automotive powertrain applications. Material Science Forum, 419-422, 57-66.

Aluminium Matter. (5. October 2011). Abgerufen am 5. October 2011 von http://aluminium.matter.org.uk/, http://aluminium.matter.org.uk/

Al-Samman, T. G., G. Gottstein. (2008). Room temperature formability of a magnesium AZ31 alloy: Examining the role of texture on the deformation mechanisms. Materials Science and Engineering A, 488, 406–414.

Avedesian, M. (1999). ASM Speicality Handbook Magnesium and Magnesium Alloys. Ohio: ASM International.

Bahadirov, K. (2010). Asymmetric Rolling of Aluminium 1050, M.Sc thesis. Aveiro: University of Aveiro.

Banabic, D. (2000). Formability of Metallic Materials. Springer-Verlag Berlin.

Barnett, M. N., N. Stanford., P. Cizek., A. Beer., Z. Xuebin (2009). Deformation mechanisms in Mg alloys and the challenge of extending room-temperature plsticity. Journal of Materials, 61, 19-23.

Barnett, M. R., Z. Keshavarz., X. Ma (2006). A semianalytical Sachs model for the flow stress of a magnesium alloy. Metallurgical and Materials Transactions A, 37A, 2283-2293.

Brown, D. S., S. R. Agnew., M. Bourke., T. Holden., S. Vogel., C. Tome (2005). Internal strain and texture evolution during deformation twinning in magnesium. Materials Science and Engineering A, 399, 1-12.

Bryla, K., J. Dutkiewicz., P. Malczewski (2009). Grain refinement in AZ31 alloy processed by equal channel angular pressing. Archives of Materials science and Engineering, 40, 17-22.

Bunge, H. (1982). Texture analysis in materials science: mathematical methods. London: Butterworth publishers.

Cahn, R. W., C. X. Shi., J. Ke (1999). Structure and Properties of Nonferrous Alloys. Beijing: Beijing, Science Press.

Choi, S. H., D. H. Kim., H. W. Lee., B. S. Seong., K. Piao., R. Wagoner (2009). Evolution of the deformation texture and yield locus shape in an AZ31 Mg alloy sheet under uniaxial laoding. Materials Science and Engineering A, 526, 38-49.

Choi, S. E., E. J. Shin., B. S. Seong (2007). Simulation of deformation twins and deformation texture in an AZ31 Mg alloy under uniaxial compression. Acta Materialia, 55, 4181–4192.

Cole, G. (2007). Magnesium vision 2020: A North American Automotive Strategic Vision of Magnesium. USAMP report.

Czerwinski, F. (2008). Magnesium Injection Molding. Springer.

Davies, G. (2003). Magnesium. Materials for Automotive Bodies. Oxford: Butterworth-Heinemann, 91, 158, 159.

Dieter, G. (1988). Mechanical Metallurgy. London: McGraw-Hill.

Duffy, L. (1996). Magnesium Alloys: The light choice for Aerospace. Materials World, 4, 127-130.

Eliezer, D., E. Aghion., F. H. Froes (1998). Magnesium science and technology. Advanced Performance Materials, 5, 201-212.

Emley, E. (1966). Principles of Magnesium Technology. Pergamon Press.

Engler, O. V. (2010). Introduction to Texture Analysis. CRC press.

Friedrich, H., S. Schumann (2001). New age of magnesium. Journal of Materials Processing Technology, 117, 276-281.

Friederich, H., E. Horst., B. L. Mordike (2006). Technology of magnesium and magnesium alloys. Magnesium Technology: Metallurgy, Design Data, Applications. Berlin: Springer.

Gao, Z. (2009). Microstuctural stability of Magnesium alloys during high temperature deformation, MASc. thesis. McMaster University, Mat Sci and Eng. Ontario, Canada: McMaster University.

Gehrmann, R., M. M. Frommert., G. Gottstein (2005). Texture effects on plastic deformation of magnesium. Materials Science and Engineering, A 395, 338-349.

Gerald, G. S. (2003). Issues that influence magnesium's use in the automotive industry. Material Science. Forum, 419-422, 43-50.

Graff, S. (2008). Micromechanical Modeling of the Deformation of HCP Metals. Hamburg: GKSS.

Hartig, C. S., A. Styczinski., F. Kaiser., D. Letzig (2005). Plastic anisotropy and texture evolution of rolled AZ31 magnesium alloys. Materials Science Forum, 495 - 497, 1615-1620.

Hielscher, R., H. Schaeben (2008). A novel pole figure inversion method: specification of the MTEX algorithm. Journal of Applied Crystallography, 41 (6), 1024-1037.

Hill, R. (1965). Continuum micro-mechanics of elastoplastic polycrystals. Journal of the Mechanics and Physics of Solids, 13, 89.

Humphreys, F., M. Hatherly (1995). Recrystallisation and Related Annealing Phenomena. Oxford: Pergamon.

Hutchinson, W. T. (1983). In E. J. N.G.Ohlson (Hrsg.), Proc. 4th International Conference of Mechanical Behaviour of Materials, (S. 1227). Pergamon Press.

Karaman, I., H. Sehitoglu., A. J. Beaudoin., Y. I. Chumlyakov., H. J. Maier., C. N. Tome (2000). Modeling the deformation behavior of Hadfield steel single and polycrystals due to twinning and slip. Acta Materialia, 48 (9), 2031-2047.

Kawalla, R., C. Schmidt., H. Riedel., A. Prakash (2007). Experimental and numerical investigation of texture development during hot rolling of magnesium alloys. Proceedings of the 7th International Conference Magnesium Alloys and their Applications. Edited by K. U. Kainer, WILEY-VCH Verlag GmbH, 274-280.

Kim, S. H., Y. M. Seo (2005). Effect of rolling conditions on the microstructure and texture evolution of AZ31 magnesium alloy sheets. Materials Forum, 29, 530-535.

Kocks, U. F. (1970). Relation between polycrystal deformation and single-crystal deformation. Metallurgical Transactions, 1 (5), 1121.

Kocks, U. (1998). Texture and Anisotropy. Cambridge: Cambridge University Press.

Koike, J. (2005). Enhanced Deformation Mechanisms by Anisotropic Plasticity in Polycrystalline Mg Alloys at Room Temperature. Metallurgical and materials transections A, 36A, 1689-1696.

Kuo, J. L., S. Sugiyama., S. H. Hsiang., J. Yanagimoto (2006). Investigating the characteristics of AZ61 magnesium alloy on the hot and semi-solid compression test. International Journal of Advanced Manufacturing Technology, 29 (7-8), 670-677.

Lawrence, E. (1975). Interfacial Phenomena in Metals and Alloys. Addison-Wesley Pub. Co.

Lebensohn, R. A., C. N. Tome (1993). A self-consistent anisotropic approach for the simulation of plastic deformation and texture development of polycrystals: Application to zirconium alloys. Acta Metallurgica et Materialia, 41 (9), 2611-2624.

Lebensohn, R. A., C. N. Tome (1994). A self-consistent viscoplastic model: prediction of rolling textures of anisotropic polycrystals. Materials Science and Engineering A, 175 (1-2), 71-82.

Lebensohn, R. A. (1997). A self-consistent approach for modelling texture development of two-phase polycrystals: Application to titanium alloys. Acta Materialia, 45 (9), 3687-3694.

Lee, B. H., S. H. Park., S. G. Hong., K. T. Park., C. S. Lee (2011). Role of initial texture on the plastic anisotropy of Mg-3Al-1Zn alloy at various temperatures. Materials Science and Engineering A, 528, 1162-1172.

Lee, S., Y. H. Chen., J. Y. Wang (2002). Isothermal formability of magnesium alloys AZ31 and AZ61. Journal of Materials Processing Technology, 124, 19-24.

Löffler, A., S. Schumann., K. U. Kainer., B. Bronfirr (2007). Examination of the forming properties of magnesium wrought alloys MRI-301F and AZ80A. 7th International Conference Magnesium and their Applications. Edited by K. U. Kainer, WILEY-VCH Verlag GmbH, 336-343.

Lopes, A. B. (2001). Análise Microestrutural das Instabilidades Plásticas em Materiais Metálicos. Aveiro, PhD Thesis: 227: University of Aveiro.

Luo, A., A. K. Sachdev (2007). Development of a new wrought magnesium-aluminum-manganese alloy AM30. Metallurgical and Materials Transactions A, 38A (6), 1184-1192.

Magnesium. http://en.wikipedia.org/wiki/Magnesium. (17. May 2011). Von www.wikipedia.com: http://en.wikipedia.org/wiki/Magnesium abgerufen

Mikroskope. www.wie-tec.de. (31. July 2011). (Metaserv) Von www.wie-tec.de: http://www.wie-tec.de/ abgerufen

Mohd Ruzi, H., M. Norhamidi., S. A. Baker., R. J. Khairul., M. N. N. Hafiez., A. Sufizar., M. I. I. Halim., Murtadhahadi (2009). A Review of workability of wrought magnesium alloys. Universiti Kebangsaan Malaysia, Department of Mechanical and Material Engineering. Bangi, Selangor: Advanced Manufacturing Research Group.

Molinari, A., G. R. Canova., S. Azhi (1987). A self-consistent approach of the large deformation polycrystal viscoplasticity. Acta Metallurgica, 12, 2983-2994.

Mordike, B. L., T. Ebert (2001). Magnesium – applications – potential. Journal of Material Science Engineering, A 302, 37-45.

Park, S. H., S. G. Hong., C. S. Lee (2010). Activation mode dependent {1 0 -1 2} twinning characteristics in a polycrystalline magnesium alloy. Scripta Materialia, 62, 202-205.

Pekguleryuz, M. O., A. A. Kaya (2003). Creep resistant magnesium alloys for powertrain applications. Advanced Engineering Materials, 5 (12), 866-878.

Pekguleryuz, M. O., E. Baril., P. Labelle (2003). Creep resistant Mg-Al-Sr alloys. Journal of Advanced Materials, 35 (3), 32-38.

Proust, G. C., C. N. Tome., A. Jain., S. R. Agnew (2009). Modeling the effect of twinning and detwinning during strain-path changes of magnesium alloy AZ31. International Journal of Plasticity, 25, 861-880.

Rauch, E. (2004). Effects of metal charateristics and experimental conditions on dislocation self-organization. La Revue de Métallurgie-CIT/Science et Génie des Matériaux , 1007-1019.

Sachs, G. (1928). Zur Ableitung einer Fleissbedingung. Zeichschrift der Verein Deutscher Ingenieur, 72, 734.

Schmitt, J. H., E. L. Shen., J. L. Raphanel (1994). A parameter for measuring the magnitude of a change of strain path: Validation and comparison with experiments on low carbon steel. International Journal of Plasticity, 10 (5), 535-551.

Schumann, S., H. Friedrich., Y. Kojima., T. Aizawa., K. Higashi., S. Kamado (2003). Current and future use of magnesium in the automobile industry. Material Science. Forum, 419-422, 51-56.

Serkan, T., F. Ozturk., I. Kacar (2008). Review of warm forming of aluminum-magnesium alloys. Journal of Materials Processing Technology, 207, 1-12.

Shen, E. (1988). PhD Thesis. Instituto Nacional Politécnico de Grenoble. Grenoble, France: Instituto Nacional Politécnico de Grenoble.

Staroselsky, A., L. Anand (2003). A constitutive model for HCP materials deforming by slip and twinning: application to magnesium alloy AZ31B. International Journal of Plasticity, 19, 1843-1864.

Styczynski, A., Ch. Hartig., J. Bohlen., D. Letzig (2004). Cold rolling textures in AZ31 wrought magnesium alloy. Scripta Materialia, 50 (7), 943-947.

Taylor, G. I. (1938). Plastic strain in metals, J. Int. Met. 62, 307.

Vieira, M. F. (1994). Solicitações Sequenciais em Cobre Policristalino: Comportamento após Pré-deformação. Tese de Doutoramento. Faculdade de Engenharia. Porto. Porto: Universidade do Porto.

Vincze, G. (2007). Investigation methodologies for metals used in forming process, PhD thesis. University of Aveiro, Department of Mechanical Engineering. Aveiro: University of Aveiro.

Wang, H., P. D. Wu., M. A. Gharghouri (2010). Effects of basal texture on mechanical behaviour of magnesium alloy AZ31B sheet. Materials Science and Engineering A, 527, 3588–3594.

Wang, Y. N., J. C. Huang (2003). Texture analysis in hexagonal materials. Materials Chemistry and Physics, 81, 11-26.

Watarai, H. (2005). Trend of research and development of Mg alloys. Science and Technology Trends, 7, 84-97.

Wei, S. C. (2006). Mechanical properties and microstructure of magnesium alloy from severe plastic deformation. Singapore: National University of Singapore.

Yang, Z., J. P. li., J. X. Zhang., G. W. Lorimer., J. Robson (2008). Review on research and development of magnesium alloys. Acta Metallurgica Sinica. (English Letters), 21 (5), 313-328.

Yi, S. (2005). Texture development in magnesium and its alloys. Investigation on the Deformation Behavior and the Texture Evolution in Magnesium Wrought Alloy AZ31. PhD thesis. Technischen Universität Clausthal.

Yi, S. B., C. H. J. Davis., H. G. Brokmeier., R. E. Bolmaro., K. U. Kainer., J. Homeyer (2006). Deformation and texture evolution in AZ31 magnesium alloy during uniaxial loading. Acta Materialia, 54 (2), 549-562.

Yoo, M. H., J. R. Morris., K. M. Ho., S. R. Agnew (2002). Non-basal deformation modes of HCP metals and alloys: Role of dislocation source mobility. Metallurgical and Materials Transactions A, 33A, 813-822.

Zaoui, A. Physique et Mécanique de la Mise en Forme des Mataux, Eds. F. Moussy and P. Franciosi, Press du CNRS, Paris, 1990, Cap. VI.4.

Appendix 1

(Crystallographic Textures – Euler space representation)

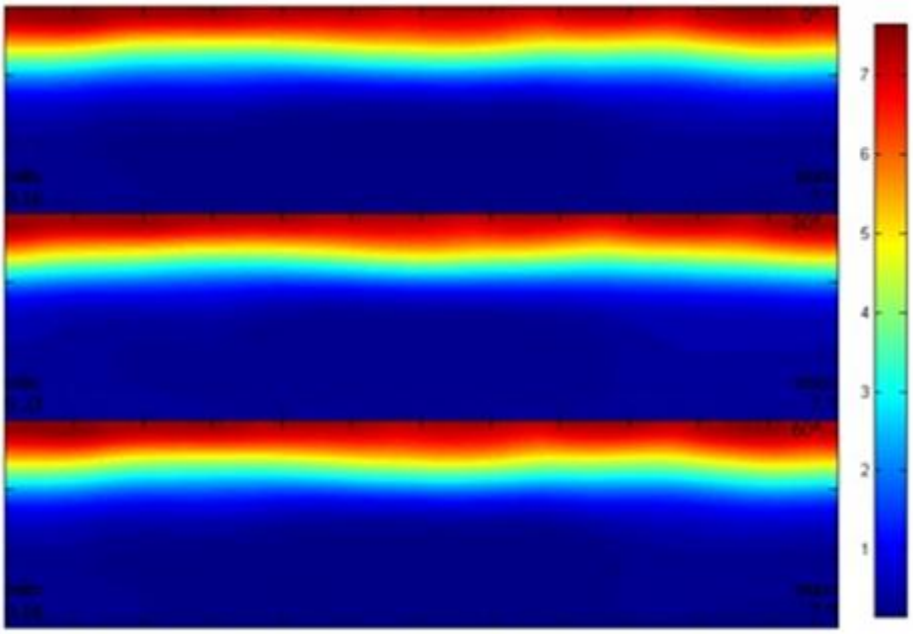

Figure A.1 – $\varphi_2 = 0^o, 30^o, 60^o$ sections of Euler space for experimental texture of the as-received material (pole figure in fig. 4.5)

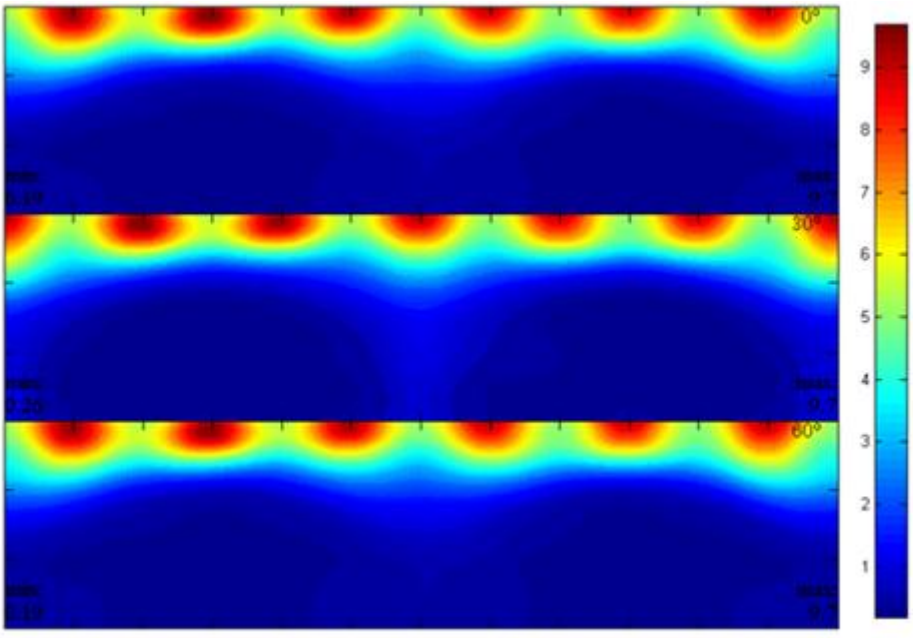

Figure A.2 - $\varphi_2 = 0^o, 30^o, 60^o$ sections of Euler space for the material after tensile test up to the maximum uniform strain at 0^o (pole figure in fig. 4.6).

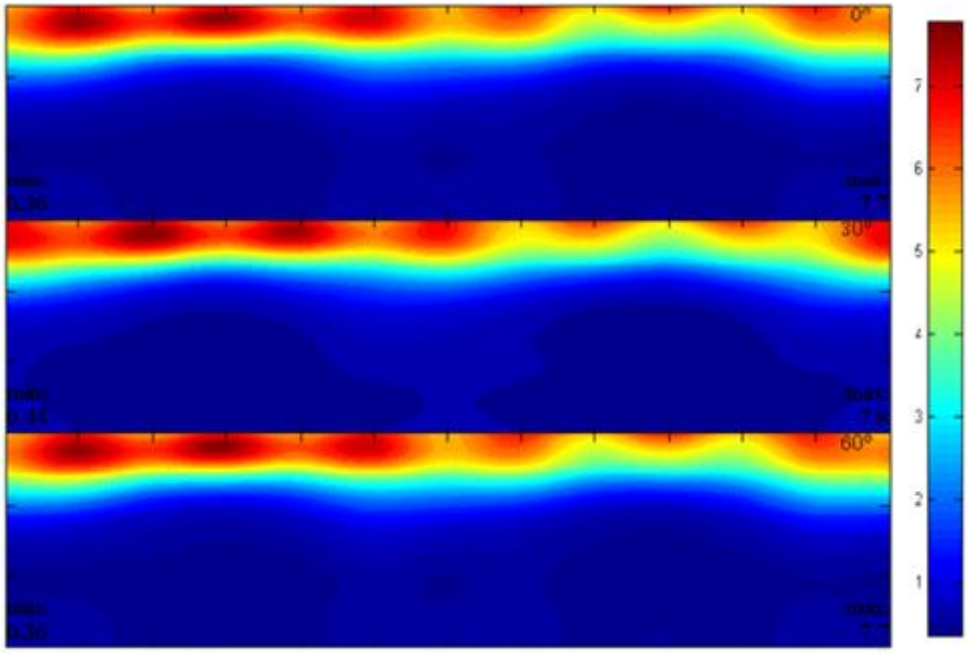

Figure A.3 - $\varphi_2 = 0^o$, 30^o, 60^o sections of Euler space for the material after tensile test up to the maximum uniform strain at 45^o (pole figure in fig. 4.7).

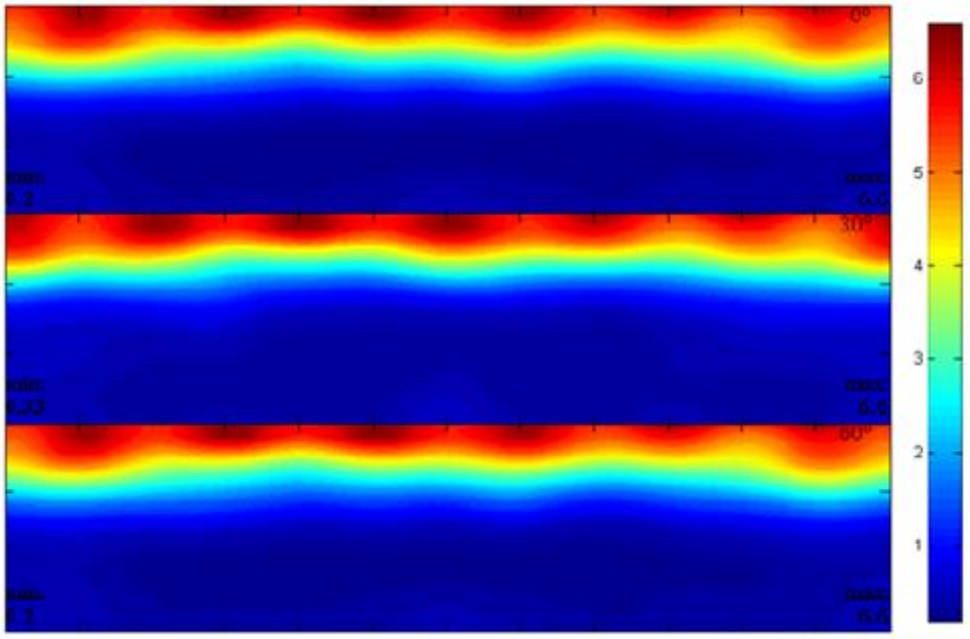

Figure A.4 - $\varphi_2 = 0^o$, 30^o, 60^o sections of Euler space for the material after tensile test up to the maximum uniform strain at 90^o (pole figure in 4.8)

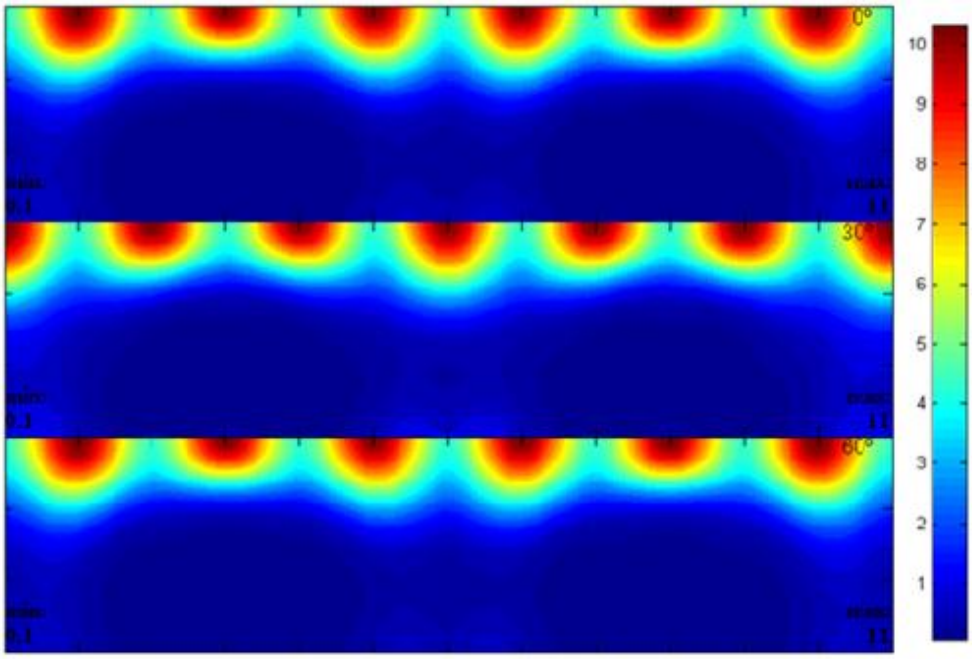

Figure A.5 - Simulated (using VPSC code) φ_2 = 0°, 30°, 60° sections of Euler space for the material after tensile test up to the maximum uniform strain at 0° (pole figure 4.9).

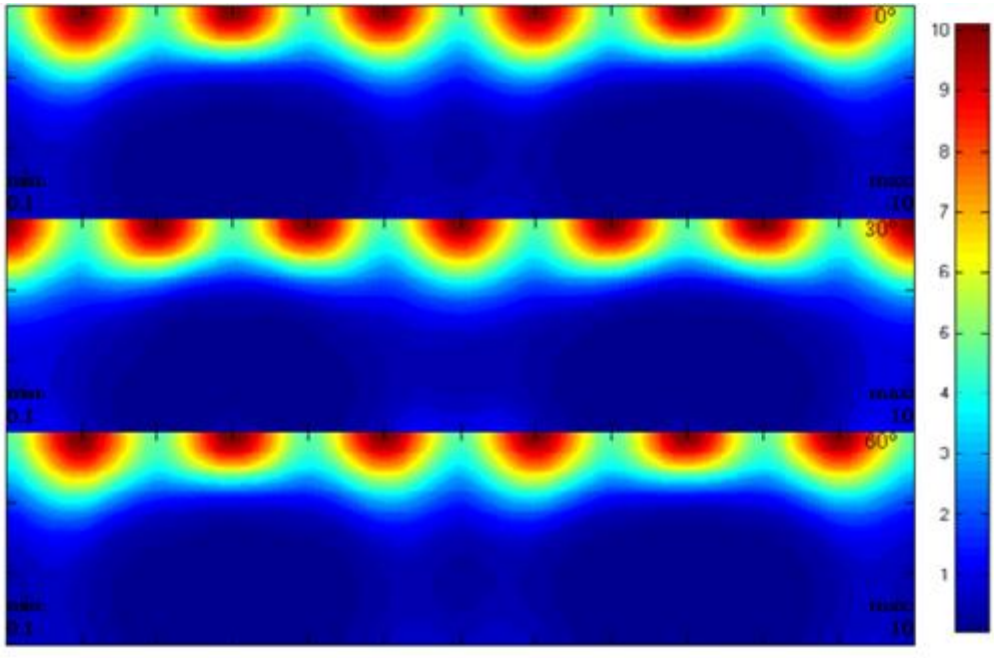

Figure A.6 - Simulated (using VPSC code) φ_2 = 0°, 30°, 60° sections of Euler space for the material after tensile test up to the maximum uniform strain at 45° (pole figure 4.10).

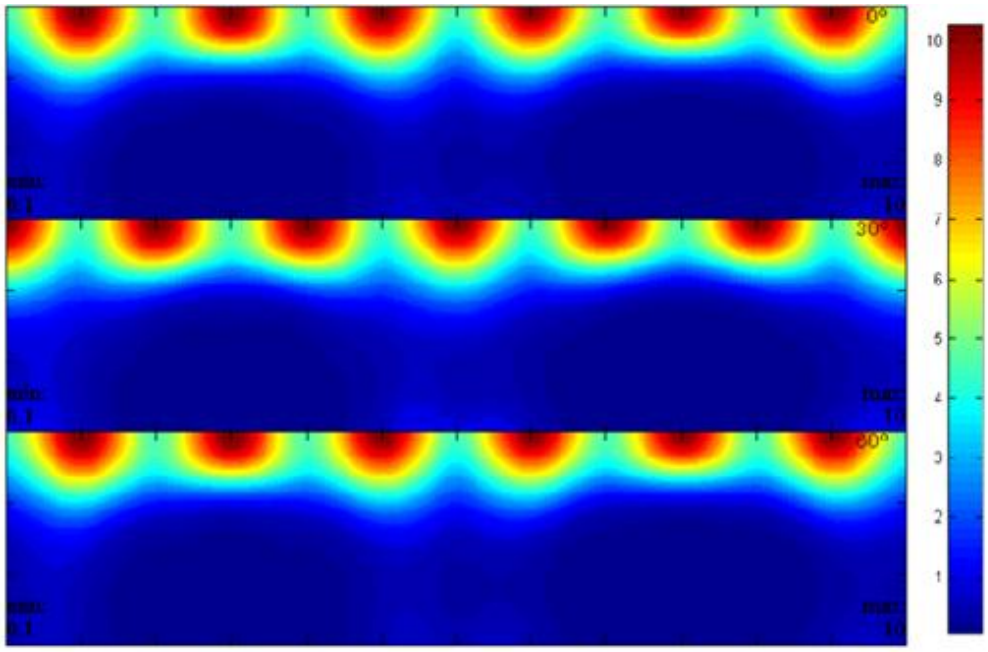

Figure A.7 – Simulated (using VPSC code) φ_2 = 0°, 30°, 60° sections of Euler space for the material after tensile test up to the maximum uniform strain at 90° (pole figure 4.11).

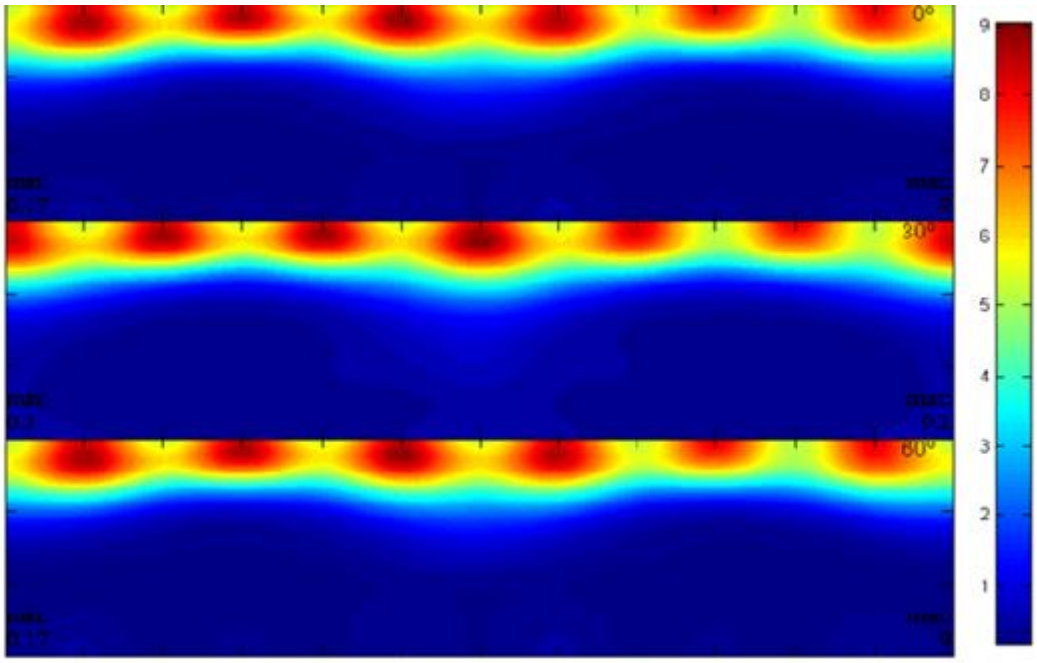

Figure A.8 - Experimental φ_2 = 0°, 30°, 60° sections of Euler space for the material after reloading at 0° (pole figure 4.16)

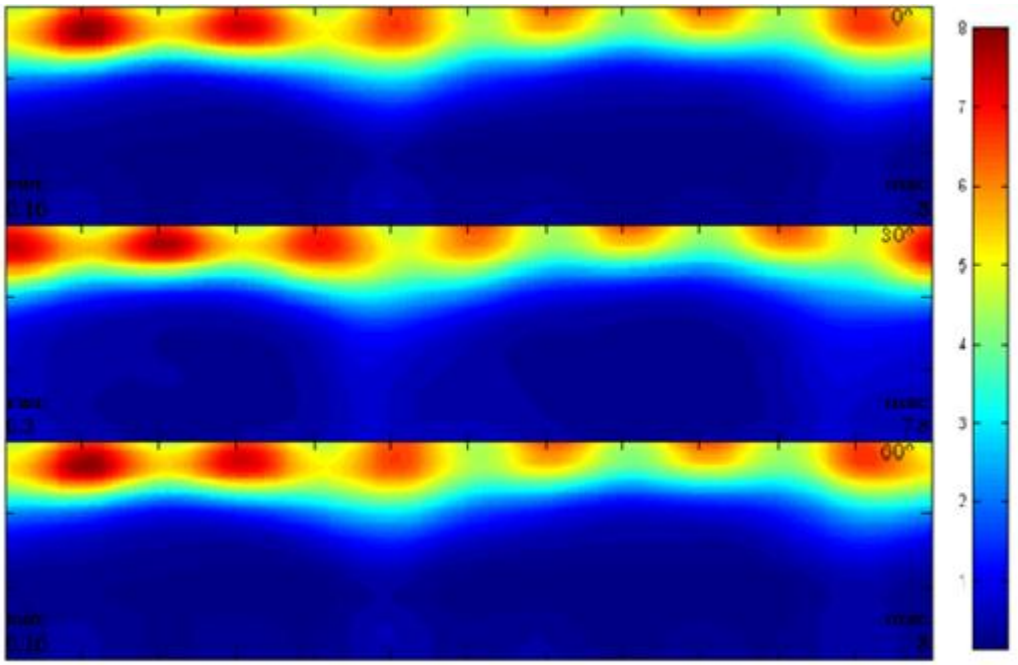

Figure A.9 - Experimental φ_2 = 0°, 30°, 60° sections of Euler space for the material after reloading at 45° (pole figure in 4.17).

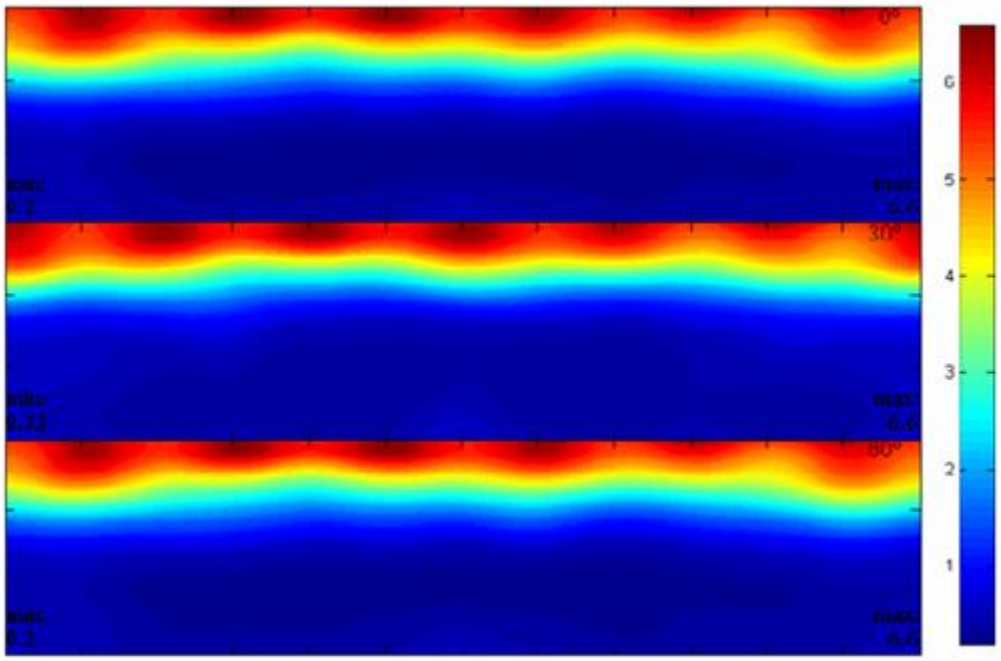

Figure A.10 - Experimental φ_2 = 0°, 30°, 60° sections of Euler space for the material after reloading at 90° (pole figure 4.18).

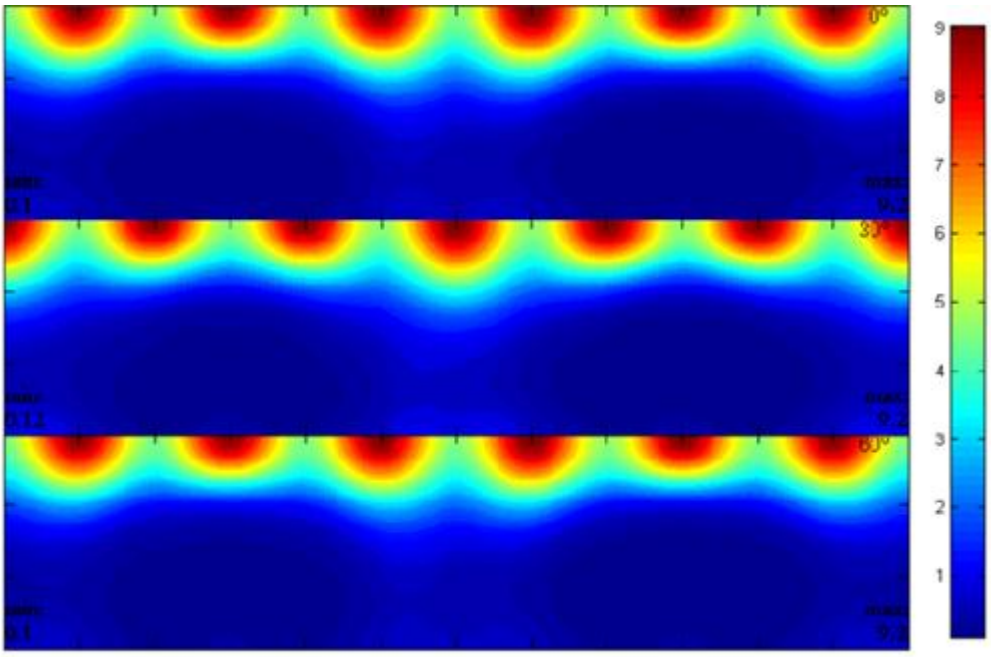

Figure A.11 - Simulated (using VPSC code) φ_2 = 0°, 30°, 60° sections of Euler space for pre-deformed (up to around 0.07) and reloaded at 0° (pole figure 4.19)

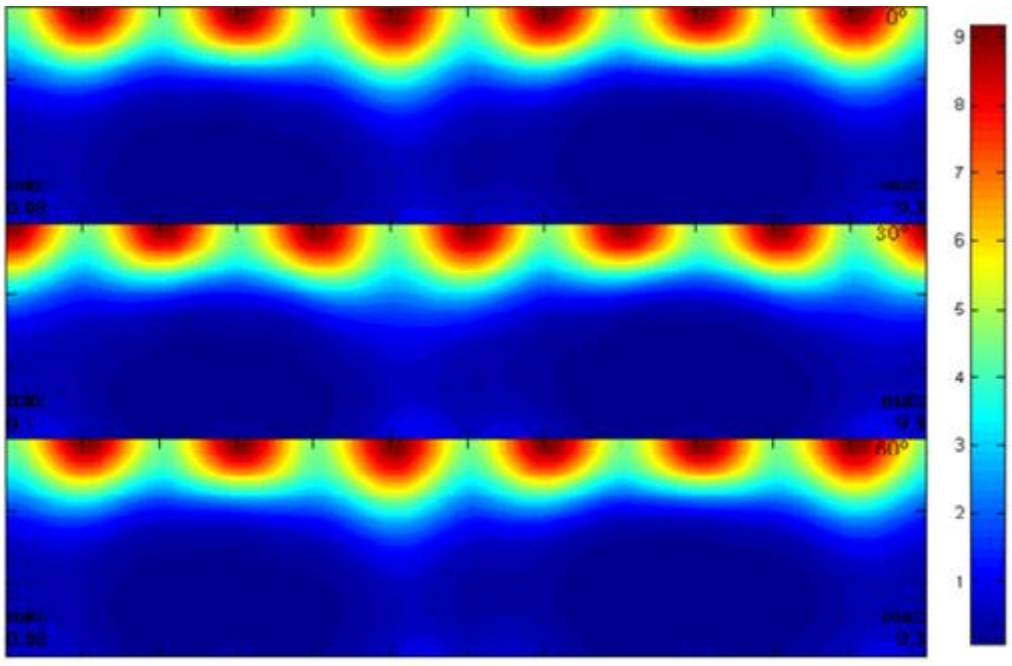

Figure A.12 - Simulated (using VPSC code) φ_2 = 0°, 30°, 60° sections of Euler space for pre-deformed (up to around 0.07) and reloaded at 45° (pole figure 4.20)

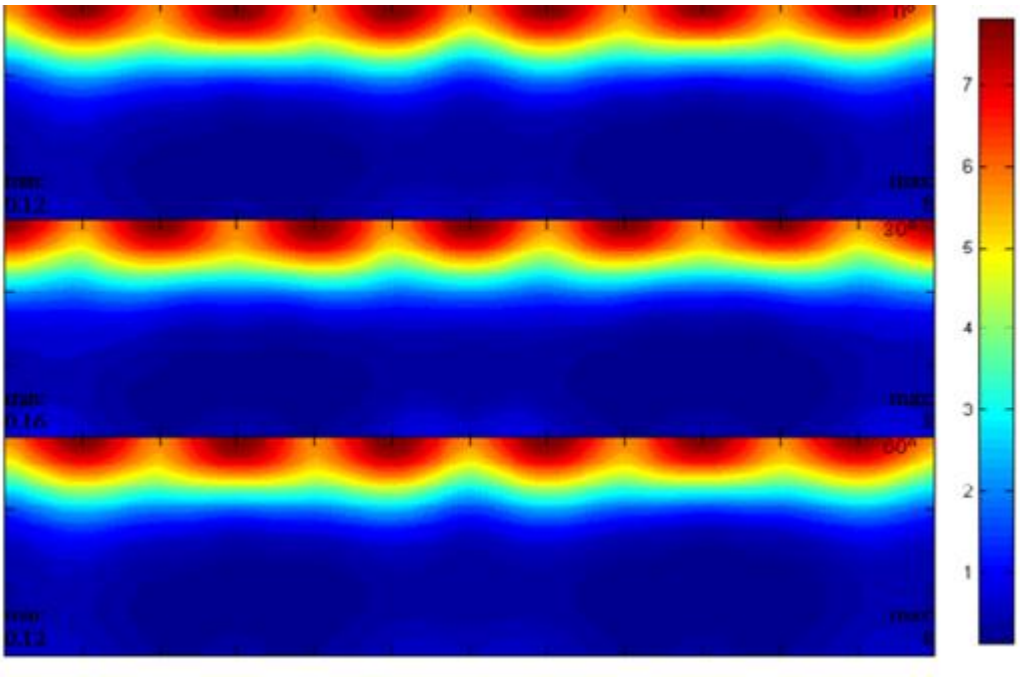

Figure A.13 - Simulated (using VPSC code) $\varphi_2 = 0^o$, 30^o, 60^o sections of Euler space for pre-deformed (up to around 0.07) and reloaded at 90^o (pole figure 4.21)

Appendix 2

(Calculation of α-parameter)

The α-value was calculated from the following equation

$$\alpha = \frac{d\varepsilon_p : d\varepsilon_r}{\sqrt{d\varepsilon_p : d\varepsilon_p}\sqrt{d\varepsilon_r : d\varepsilon_r}} \tag{A.1}$$

In the above equation the ε_p and ε_r are the pre-deformation and the reloading strain tensors respectively.

For tensile test $\varepsilon_{ij} = 0$ when $i \neq j$ and, therefore:

$$\varepsilon_p = \begin{bmatrix} \epsilon_{11} & 0 & 0 \\ 0 & \epsilon_{22} & 0 \\ 0 & 0 & \epsilon_{33} \end{bmatrix} \tag{A.2}$$

For a reloading tensile test at an angle θ away from the pre-deformation tensile direction, the reloading strain tensor is given by:

$$\varepsilon_r = \begin{bmatrix} \varepsilon'_{11}\cos^2\theta + \varepsilon'_{22}\sin^2\theta & (\varepsilon'_{22} - \varepsilon'_{11})\cos\theta\sin\theta & 0 \\ (\varepsilon'_{22} - \varepsilon'_{11})\cos\theta\sin\theta & \varepsilon'_{11}\cos^2\theta + \varepsilon'_{22}\sin^2\theta & 0 \\ 0 & 0 & 0 \end{bmatrix} \tag{A.3}$$

and

$$\varepsilon_p : \varepsilon = (\varepsilon_{11}\varepsilon'_{11} + \varepsilon_{22}\varepsilon'_{22})\cos^2\theta + (\varepsilon_{11}\varepsilon'_{22} + \varepsilon_{22}\varepsilon'_{11})\sin^2\theta \tag{A.4}$$

$$\varepsilon_p : \varepsilon_p = \varepsilon_{11}^2 + \varepsilon_{22}^2 + \varepsilon_{33}^2 \tag{A.5}$$

$$\varepsilon_r : \varepsilon_r = \varepsilon'^2_{11} + \varepsilon'^2_{22} + \varepsilon'^2_{33} \tag{A.6}$$